UNIVERSIDADE DE SÃO PAULO
ESCOLA DE ENGENHARIA DE SÃO CARLOS

LUCAS KONAKA NOLASCO

Investigation of the fs-laser micromachining process in GaN and diamond

São Carlos
2021

LUCAS KONAKA NOLASCO

Investigation of the fs-laser micromachining process in GaN and diamond

Corrected Version

Dissertation presented to the Graduate Program in Materials Science and Engineering at São Carlos School of Engineering, University of São Paulo, to obtain the degree of Master of Science.

Concentration Area: Development, Characterization and Application of Materials.

Advisor:
Prof. Dr. Cleber Renato Mendonça

São Carlos
2021

Catalog card prepared by Patron Service at "Prof. Dr. Sergio Rodrigues Fontes" Library at EESC/USP

N789i

Nolasco, Lucas Konaka
Investigation of the fs-laser micromachining process in GaN and diamond / Lucas Konaka Nolasco; promoters Cleber Renato Mendonça. -- São Carlos, 2021.

Master (Dissertation) - Graduate Program in Materials Science snd Engineering and Research Area in Development, Characterization and Application Materials of the School of Engineering of São Carlos at University of São Paulo, 2021.

1. Fs-Micromachining. 2. Nonlinearoptics. 3. Wide bandgap semiconductor. 4. Incubation effect. 5.GaN. 6. CVD diamond. I. Title.

Elena Luzia Palloni Gonçalves – CRB 8/4464

FOLHA DE JULGAMENTO

Candidato: Bacharel **LUCAS KONAKA NOLASCO.**

Título da dissertação: " Investigação do processo de microfabricação via pulsos ultracurtos no GaN e diamante".

Data da defesa: 19/02/2021.

Comissão Julgadora	**Resultado**
Prof. Titular **Cleber Renato Mendonça** **(Orientador)** (Instituto de Física de São Carlos/IFSC-USP)	APROVADO
Prof. Dr. **Sebastião Pratavieira** (Instituto de Física de São Carlos/IFSC-USP)	APROVADO
Prof. Dr. **Antonio Riul Júnior** (Universidade Estadual de Campinas/UNICAMP)	APROVADO

Coordenador do Programa de Pós-Graduação em Engenharia de Materiais:
Prof. Associado **Marcelo Falcão de Oliveira**

Presidente da Comissão de Pós-Graduação:
Prof. Titular **Murilo Araujo Romero**

Dedicated
to my family and friends,
for all the love and support.

ACKNOWLEDGMENTS

Firstly, I would like to thank my advisor Prof. Dr. Cleber Renato Mendonça, for all the support not only while I was working on this master's degree, but during my undergraduate years as well. He is an exceptional advisor, always able to create an incredibly positive and cooperative atmosphere within the Photonics Group at IFSC-USP, and willing to help his students or introducing us to someone else who can.

I would like to thank my colleges and friends, current or ex-members of the Photonics Group for the shared experiences, advice and overall camaraderie: Franciele Renata Henrique, Nathália Beretta Tomazio, Henry Passagem, Gustavo Foresto Brito de Almeida, Sabrina Nicoleti C. dos Santos, Kelly Tasso, Leandro Cocca, Lucas Sciuti, Juliana Almeida, Adriano Otuka, André Pelosi, Danyellen Galindo, Luiz Eduardo Rocha, Kauê Lima Curvelo da Silva, Rafael Garcia, Gabriela Flores, Beatriz Costa Menezes, Mario Buozzi, as well as Prof. Dr. Leonardo de Boni, and Prof. Dr. Lino Misoguti.

Thanks to the Photonics Group staff Daniel Foschini Pereira for a fantastic job as Secretary, and André Romero for all the technical support.

I wish to express my gratitude towards all my friends and specially my girlfriend Cristiane London for all the emotional support and for being there for most of the tough and happy moments.

I would like to thank my parents Andréia and Arnaldo and my family for the unconditional love, patience and support.

Lastly, I am grateful to the Air Force Office of Scientific Research for the financial support.

“If I have seen further
it is by standing
on the shoulder of Giants.”

Isaac Newton

ABSTRACT

NOLASCO, L. K. **Investigation of the fs-micromachining process in GaN and diamond.** Dissertation (Master of Science) - Escola de Engenharia de São Carlos, Universidade de São Paulo, São Carlos, 2021.

Semiconductor materials are essential for novel technology development in optoelectronic and photonic devices. Among these types of materials, diamond and GaN stand out given their high bandgap and optimal electronic and thermal properties. Amidst the many material processing techniques, the femtosecond laser pulses micromachining is employed due to its high precision and ability to create microstructures either on the surface or bulk of a material. Thus, in this dissertation, we have studied the fundamentals of fs-micromachining process in both GaN and CVD diamond at 343, 515 and 1030 nm. More specifically, we have examined the incubation effect: the damage threshold fluence (minimal fluence necessary to produce damage in the material) decreases with the number of femtosecond pulses applied per sample spot. The threshold fluence was determined through the zero damage method, which consists of using Gaussian intensity profiles with distinct energies in a material surface. Hence, the incubation curves were obtained for both materials and were fitted by an exponential defect model, which correctly predicts the saturation of the threshold fluence observed in the high-pulse superposition region. The model also indicates through its incubation parameter (k) the efficiency by which the fluence reaches the saturation: the higher its value, the less pulses are necessary. For the GaN sample, k = (0.4 ± 0.2) for 343 nm, k = (0.07 ± 0.01) for the green (515 nm) and k = (0.02 ± 0.01) for the IR case (1030 nm). In CVD diamond: k = (0.13 ± 0.04) for the UV, k = (0.3 ± 0.1) for 515 nm and k = (0.14 ± 0.03) for the 1030 nm excitation wavelength. A theoretical model, which assumes that only multiphoton and avalanche absorption are present, was used to compare its results of the single pulse damage threshold fluence to our experimental data. Through a numerical simulation based on this model, we determined the threshold fluences for GaN at all wavelengths, resulting in a satisfactory agreement to most experimental data, except at 1030 nm. This discrepancy was explained by determining the Keldysh parameter, which indicated that both multiphoton and tunneling absorption are present at this wavelength in GaN – a process that is not considered by the model. As for the CVD diamond, we also established good results for the UV (343 nm) and green (515 nm) excitation wavelengths, but due to the lack of absorption cross-section data at 1030 nm (required for the simulation), we resorted to an alternative method using the same model to determine the five-photon absorption cross-section (σ_5), resulting in $\sigma_5 = 5\times10^{-170}$ $m^{10}s^4photon^{-4}$, which is in good agreement with other five-photon absorption cross-sections of other materials in the literature. Hence, this study could prove important in improving the femtosecond micromachining processing technique in both GaN and diamond.

Key-words: Fs-micromachining. Nonlinear optics. Wide bandgap semiconductor. Incubation effect. GaN. CVD diamond.

RESUMO

NOLASCO, L. K. **Investigação do processo de microfabricação via pulsos ultracurtos no GaN e diamante.** Dissertação (Mestrado) – Escola de Engenharia de São Carlos, Universidade de São Paulo, São Carlos, 2021.

Materiais semicondutores são essenciais para o desenvolvimento de novas tecnologias em dispositivos optoeletronicos e fotônicos. Dentre esse tipo de material, o diamante e o GaN se destacam devido a sua banda larga e interessantes propriedades eletrônicas e térmicas. Dentre as várias técnicas de processamento de materiais, a microfabricação via pulsos de femtosegundos é empregada devido a sua alta precisão e habilidade de fabricar microestruturas tanto na superfície como no volume de materiais. Portanto, nesta dissertação nós estudamos os aspectos fundamentais do processo de microfabricação via pulsos de femtosegundos no GaN e diamante CVD em 343, 515 e 1030 nm. Mais especificamente, examinamos o efeito de incubação: o limiar de fluência de dano (fluência mínima necessária para causar dano na superficie de um dado material) decresce com o aumento do número de pulsos de femtosecundos aplicados num mesmo ponto. A fluência de limiar foi determinada através do método de dano zero, o qual consiste em aplicar perfis de intensidades Gaussianos com energias distintas na superficie de um material. Assim, as curvas de incubação foram obtidas para ambas amostras e ajustadas pelo modelo de defeito exponencial, o qual previu corretamente a saturação da fluência de limiar na região de alta sobreposição de pulsos. Esse modelo ainda indica, através do parâmetro de incubação (k), a eficiência pelo qual a fluência atinge a sua saturação: quanto maior o seu valor, menos pulsos são necessários. Para a amostra de GaN, k = (0.4 ± 0.2) em 343 nm, k = (0.07 ± 0.01) em 515 nm e k = (0.02 ± 0.01) para o caso do infravermelho (1030 nm). No diamante CVD: k = (0.13 ± 0.04) no UV (343 nm), k = (0.3 ± 0.1) para o verde (515 nm) e k = (0.14 ± 0.03) para a excitação em 1030 nm. Um modelo teórico, que assume que apenas a absorção multifotônica e avalanche ocorrem, foi utilizado com o intuito de comparar os resultados simulados da fluência de limiar de um pulso único com os dados experimentais obtidos. Através de uma simulação numérica baseada neste modelo, nós determinamos os valores da fluência de limiar de nado do GaN para todos os comprimentos de onda, resultando numa concordância satisfatória com a maioria dos dados experimentais, exceto em 1030 nm. Tal discrepância foi explicada pela determinação do parâmetro de Keldysh, que indicou que tanto a absorção via tunelamento quanto multifotônica estão presentes neste comprimento de onda no GaN – um processo não considerado pelo modelo. Já para o diamante, também estabelecemos bons resultados para a excitação em UV (343 nm) e verde (515 nm), mas devido à falta de dados sobre a secção de choque de absorção de cinco fótons (necessários para a simulação) na literatura, nós recorremos a um método alternativo utilizando o mesmo modelo para determinar a secção de choque de absorção de cinco fótons do diamante (σ_5), resultando em $\sigma_5 = 5\times10^{-170}$ $m^{10}s^4$fóton^{-4}, o que está de bom acordo com as secções encontradas na literatura de outros materiais. Desse modo, este estudo pode se provar ser importante para a melhora da técnica de microfabricação via pulsos de femtosegundos tanto no GaN quanto no diamante.

Palavras-chave: Microfabricação. Óptica não-linear. Semicondutores de banda larga. Efeito de incubação. GaN. Diamante CVD.

LIST OF FIGURES

LIST OF TABLES

LIST OF ABREVIATIONS AND ACRONYMS

CB	Conduction Band
CPA	Chirped Pulse Amplification
CVD	Chemical Vapor Deposition
EDM	Electron Discharge Micromachining
FIB	Focused Ion Beam
IFSC	Instituto de Física de São Carlos
IR	Infrared
LED	Light Emitting Diode
LENA	Laboratory for Emerging Nanometrology
LIPSS	Laser Induced Periodic Surface Structures
NA	Numerical Aperture
NBE	Near Band Emission
NV	Nitrogen Vacancy
PA	Photon Absorption
SEM	Scanning Electron Microscopy
USP	Universidade de São Paulo
UV	Ultraviolet
VB	Valence Band
WBG	Wide Bandgap

LIST OF SYMBOLS

ν_q	Laser cavity frequency regime
c	Speed of light
L	Laser cavity length
J	Total number of modes
φ_q	Phase of an electric field *q*
E_q	Amplitude of an electric field *q*
$\vec{P}$	Induced polarization
ε_0	Vacuum permittivity
$\chi^{(n)}$	*n*-order susceptibility
$\vec{E}$	Electric field
n'	Refractive index
n_2	Nonlinear refractive index
I	Laser intensity
h	Plank's constant
ν	Frequency of light
E_g	Energy gap
γ_K	Keldysh parameter
e	Electron charge
m_e	Electron mass
I_0	Laser peak intensity
ρ	Pulse spatial radius
τ	Pulse temporal radius
F	Fluence
F_0	Peak fluence
r_{th}	Threshold radius
w_0	Gaussian beam waist at the focus
E_p	Pulse energy
F_{th}	Threshold fluence
E_{th}	Threshold energy
$\bar{p}$	Average power
f	Pulsed laser repetition rate
N	Pulse superposition number

ϑ_3	Jacobi theta function
V	Scanning speed
$F_{th,N}$	Threshold fluence of *N* pulses
k	Incubation parameter
n	Produced electron number density
σ_m	*m*-photon absorption cross-section
λ	Wavelength of light
m	Number of photons of the multiphoton ionization process
N_s	Solid atom density
$\frac{2}{\alpha}$	Scale fluence
n_{cr}	Critical electron density
d	Density
N_A	Avogadro's number
M	Molecular mass
T	Transmittance

SUMMARY

1. INTRODUCTION

The necessity for miniaturized technologies has grown over the past decades, initiated by microelectronics, telecommunications, medicine amidst many other areas of research and industry[1,2]. This prompted the development of a large number of different micromachining processing techniques such as EDM (Electron Discharge Micromachining), a method that consists of utilizing an electrode close to a conducting material's surface submerged in a dielectric fluid, causing the removal of matter through melting and evaporation[3,4], FIB (Focused Ion Beam), where as the name implies, an ion beam is tightly focused on the surface of a material (10-500 nm spot sizes), consequently etching it[5], and among them, the femtosecond micromachining technique, utilizing fs-laser pulses.

Figure 1 – Fs-micromachined structures: 3-D structure made by 2-photon polymerization (a), super-hydrophobic surface (b) and a waveguide fabricated in Gorilla Glass (c).

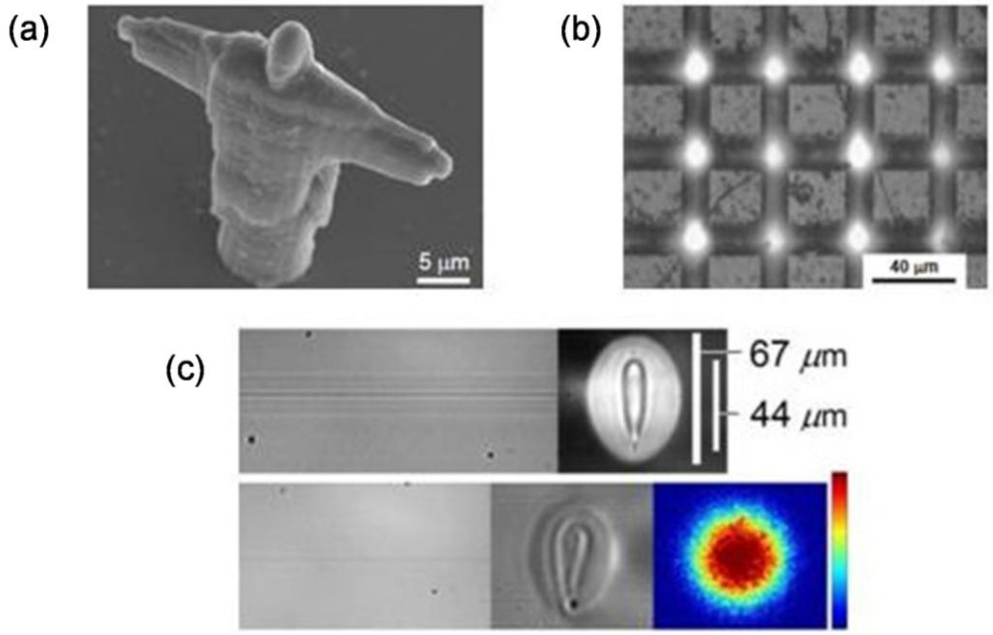

Source: adapted from IFSC USP-Photonics Group (a,b) and Lapointe, et al.[6](c).

Since its development in 1960[7], the laser has been applied in many areas of research as a fundamental material processing tool. As such, it was unavoidable that it would suffer many technological advances throughout the years, one of which being the production of pulsed lasers of femtosecond (10^{-15} s) pulse duration. Femtosecond lasers can generate extremely short and intense pulses,

which cause thermal effects significantly smaller when compared to lasers with longer pulse duration, paving the way for the so-called femtosecond laser micromachining research area in photonics, which consists of producing micrometric structures in the surface or bulk of a material (seen in Fig. 1) with great precision via optical breakdown, a process that causes permanent damage through energy transferred from the optical field to the material, causing a local ionization of a large number of electrons[8], as the high peak intensities are able to achieve the nonlinear optical regime.

Semiconductor materials are essential for advances in new technologies regarding electronics and optoelectronics devices. Among them, wide bandgap (WBG) semiconductors (semiconductors with bandgap value greater than 2.2 eV[9]) stand out given their typical high hole mobility ratio, electron mobility, and thermal conductivity, making them ideal materials for novel technology[10]. GaN (Gallium Nitride) and diamond, both classified as WBG semiconductors, are considered to be the most promising semiconductors to achieve new technological development in many different areas of research. Naturally, many different processing methods have been used in these materials, and among them, the femtosecond laser micromachining, due to its high precision as mentioned before, thus generating several studies related to this field.

Tens-of-micrometers order structures were first produced in GaN by an Ti:sapphire laser at 800 nm with 100 fs pulses[11]. The structures had their depths measured, and determined a fluence threshold (the minimal fluence necessary to produce damage) of 0.3 J/cm² by analyzing the ablated depth as a function of the laser fluence. LIPSS (light-induced periodic surface structures), a phenomenon that can occur due to interactions of laser pulses with materials[12–14], were observed in GaN through the use of a Ti:sapphire laser operating at 780 nm with 150 fs pulses, as a mean of further analyzing the fs-laser damage mechanism[15]. As GaN is a good candidate for integrated optics[16–19], Bragg gratings were produced on its surface by employing a phase mask in conjunction with a Ti:sapphire laser system that produces 800 nm pulses with 35 fs of duration[20]. More recently, the incubation effect of GaN at 800 nm was studied using Ti:sapphire lasers (120 fs at 1 KHz and 50 fs at 5 MHz)[21], where it was noticed that the damage fluence threshold decreases with the increase of pulse superposition.

In diamond, the ultrashort pulsed laser was compared to longer pulses

systems, showing that when fs-pulses are employed (Ti:sapphire laser at 825 nm and 120 fs pulse duration), more precise structures are formed[22]. The influence of experimental parameters such as laser power and scanning speed on the microgrooves produced by a Nd:YLE femtosecond laser at 800 nm with 120 fs pulses were determined on CVD diamond[23]. Bulk microstructures in CVD diamond were produced by a Ti:sapphire laser at 800 nm with 120 fs pulses, as well as an incubation study demonstrating the effect of the number of shots on the damage threshold fluence[24]. More recently, the graphitization of diamond during the micromachining process was studied with an 120-fs laser centered at 800 nm, where a spectrometer was used to characterize the change of the elements before and after the laser irradiation[25]. In addition, given the diamond suitability for integrated photonics, mid-IR waveguides were produced in a single crystal diamond by a Yb:KGW fs-laser system at 515 nm with 230 fs pulses[26].

Microstructures produced via femtosecond laser micromachining are highly dependent on experimental parameters, such as laser power, translation speed of the sample, wavelength and pulse duration. For instance, the single-shot threshold fluence of fused silica is directly proportional to the increase in pulse duration[27]: ranging from ~4 J/cm² to ~7 J/cm² when the pulse increases from ~200 fs to ~800 fs. Thus, even though there are many studies regarding femtosecond micromachining in GaN and diamond, it is still an ongoing process. In particular, the incubation cumulative effect has not been thoroughly reported, as most were studied through the use of Ti:sapphire laser systems at 800 nm and ~100 fs pulses.

Thus, in this dissertation, the aim is to study the femtosecond-laser micromachining processing in Gallium Nitride and diamond at different wavelengths (1030 nm, 515 nm and 343 nm) in order to have a better understanding of the fundamentals regarding the technique such as the incubation effect: a cumulative behavior observed when multiple fs-pulses are in place during the micromachining process. The further chapters of the dissertation will treat the fundamental theories behind the experimental process (Chapter 2), addressing ultrashort laser pulses generation, nonlinear optics and the processes involved in the fs-micromachining. Soon after, in Chapter 3, all the experimental procedure will be explained, as well as the setup utilized for the study. Finally in Chapter 4, we will present all the results obtained, regarding the incubation effect, followed by a theoretical model which will

be used to simulate and compare it to the experimental results. Lastly Chapter 5 will address the conclusions and perspectives.

2. THEORETICAL BASIS

In this chapter, we will cover all relevant theoretical basis for the understanding of the experimental setup, results and further discussions in this dissertation. It will cover ultrashort pulse generation, nonlinear optical effects and finally the fs-micromachining process.

2.1. Ultrashort laser pulses

Ultrashort laser pulses are defined as light pulses ranging from picoseconds (10^{-12} s) to femtoseconds (10^{-15} s) of duration, having an extremely high pulse peak intensity. For one to be generated, it requires a gain medium (excited by a pump source), with a broad emission bandwidth as the shorter the pulse, the broader it must be in frequency. Secondly, there must be dispersion compensation elements such as a prism pair, since pulses tend to disperse in time as different light frequencies moves at different speeds and finally, there must be a mode-locking mechanism[28].

A laser cavity, composed by mirrors, allow only certain frequency regimes (ν_q), described as

$$\nu_q = q\frac{c}{2L} \tag{2.1}$$

where q is an integer, c is the light speed and L is the cavity length. As noted by this equation, there are an infinite number of modes possible in the cavity. However, in fact, the number of modes is controlled by the gain medium, which emits a broad spectrum of light when excited, actively selecting the number of oscillating frequencies in the cavity. Considering a situation in which one have a highly excited cavity, the laser output is given by as the sum of all propagating fields, as

$$E(t) = \sum_{q=1}^{J} E_q exp\left[-i\left(2\pi\nu_q t + \varphi_q\right)\right] \tag{2.2}$$

where J is the total number of modes in the cavity, E_q is the amplitude, t is the time and ν_q and φ_q are their frequencies and phases respectively.

Thus, as many different modes are possible in the cavity, an ultrashort pulse is not yet able to be formed, since there will be competition between them, resulting in fluctuations in the phases and intensities of the modes[29].

Figure 2 – Influence of the number of modes on the pulse peak intensity.

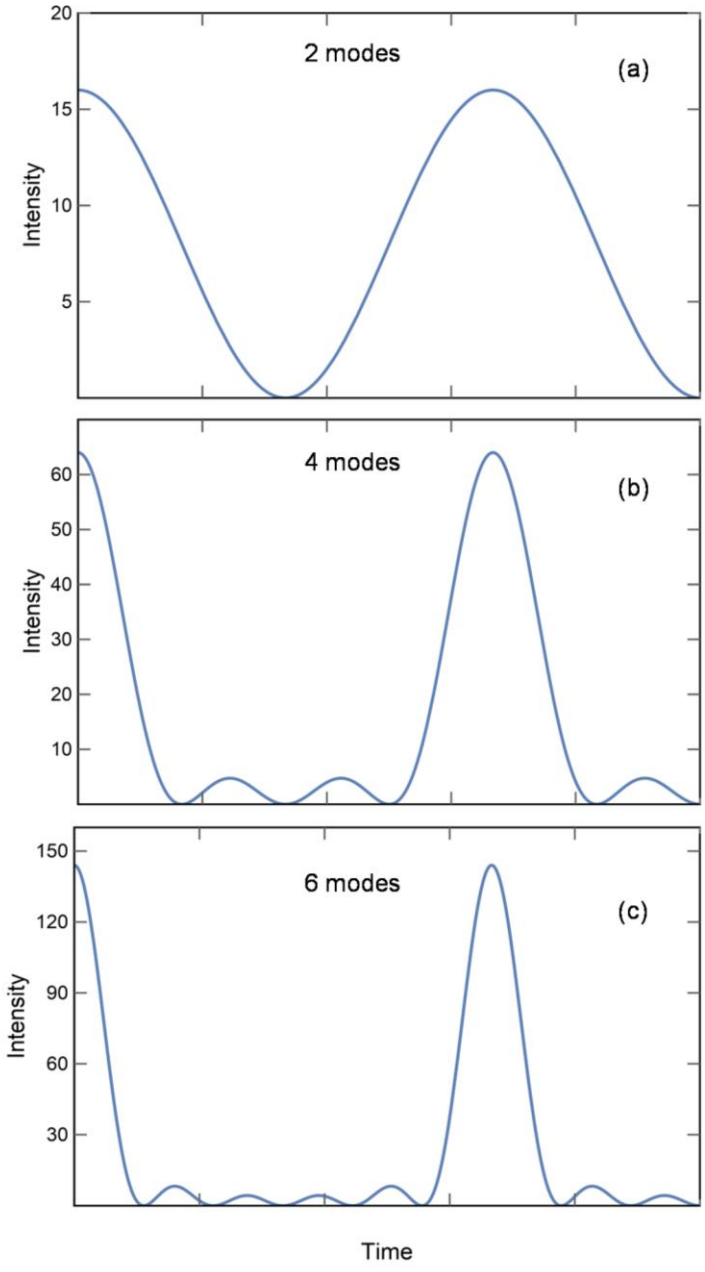

Source: by the author.

That is when the mode-locking mechanism is used: essentially it organizes the modes by making the relative phase between them (φ_q) constant, thus producing a constructive interference among them and creating exceedingly intense and short pulses, as illustrated in Fig. 2 by graphs of the light intensity, which is

proportional to the squared electric field, in function of time. In addition, it can also be concluded from Fig. 2 (a) to (c) that with the increase of the total number of modes (J), the generated mode-locked pulses become increasingly shorter, thus eventually being able to reach the femtosecond order of duration mark and ~MW peak power.

Among the many types of femtosecond lasers systems developed since its invention, one stood out for being able to increase its pulse energy from nJ to mJ, with average powers of ~W [2]: the Chirped Pulse Amplification (CPA) system[30]. This technique, which recently won a Nobel Prize in 2018, consists of stretching a low-energy pulse temporally, generated by a mode-locked laser, through diffraction gratings, as different pulse frequencies will travel distinct lengths. Then, the stretched pulses are directed to an amplifier, consisting of a gain medium. The reason why the pulse is only amplified after it is stretched is due to the fact that it will have a lower peak intensity momentarily, reducing the chances of damaging the optical components of the system. Finally, the amplified pulse is compressed by a second pair of diffraction gratings, generating an ultrashort pulse with even greater peak intensities. The whole CPA process is summarized in Fig. 3.

Figure 3 – Simplified model of a Chirped Pulse Amplification technique.

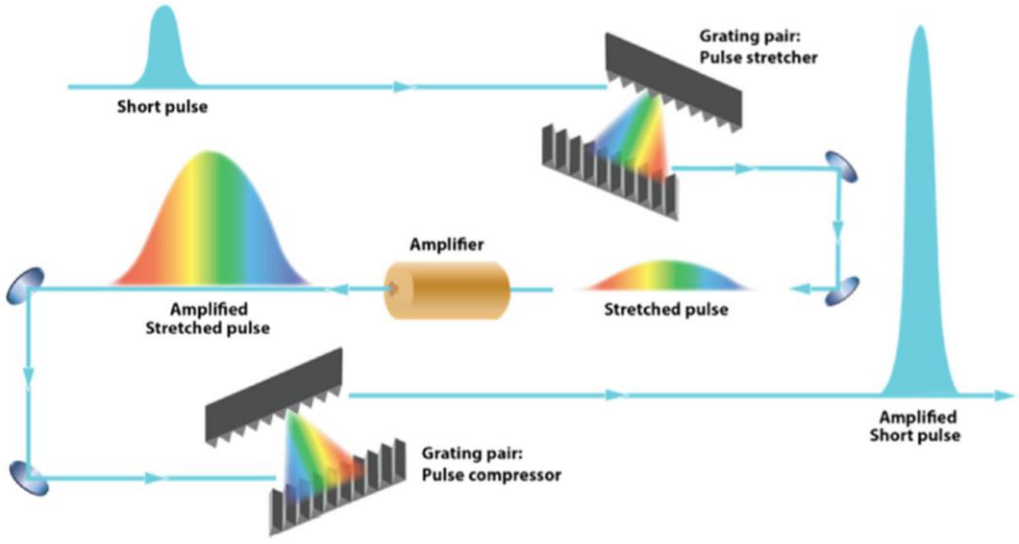

Source: adapted from Asplund, et al. [31]

2.2. Nonlinear optics

Given the extremely high peak intensity of the ultrashort laser pulses discussed in the previous section, its electric field amplitude is about the same order

of magnitude of the interatomic electric field (~10^8 V/m). Thus, the light-matter interaction can no longer be treated as in the linear optical regime, entering the nonlinear optical one. This nonlinearity comes from the fact that the response of a material behaves in a nonlinear manner on the optical field[32].

In the linear optics regime, the induced polarization depends linearly on the electric field strength[32], described by

$$\vec{P}(t) = \varepsilon_0 \chi^{(1)} \vec{E}(t), \tag{2.3}$$

where ε_0 is the vacuum permittivity and $\chi^{(1)}$ is the linear susceptibility.

In the nonlinear regime, Eq. 2.3 needs to be modified once the Drude-Lorentz model that classically treats the atom as a harmonic oscillator is no longer valid, having the necessity to be modified by treating it as an anharmonic oscillator[32]. Thus, it is usually expressed as a power series given by

$$\vec{P}(t) = \varepsilon_0 [\chi^{(1)} \vec{E}(t) + \chi^{(2)} \vec{E}^2(t) + \chi^{(3)} \vec{E}^3(t) + \cdots], \tag{2.4}$$

where $\chi^{(2)}$ and $\chi^{(3)}$ are the second and third-order nonlinear optical susceptibilities, respectively.

By analyzing Eq. 2.4, it is clear that its first term is the linear induced polarization (Eq. 2.3). Thus, we can simplify the nonlinear induced polarization as the sum of the linear ($\overrightarrow{P_L}$) and nonlinear ($\overrightarrow{P_{NL}}$) portions given by

$$\vec{P}(t) = \overrightarrow{P_L} + \overrightarrow{P_{NL}}\,, \tag{2.5}$$

where

$$\overrightarrow{P_{NL}} = \varepsilon_0 \left[\chi^{(2)} \vec{E}^2(t) + \chi^{(3)} \vec{E}^3(t) + \cdots\right], \tag{2.6}$$

which can be simplified to

$$\overrightarrow{P_{NL}} = [\overrightarrow{P^{(2)}} + \overrightarrow{P^{(3)}} + \cdots]\,. \tag{2.7}$$

Each nonlinear optical susceptibility is responsible for many different

nonlinear phenomena. The second-order nonlinear susceptibility, for instance, is responsible for second harmonic generation and sum and difference frequency generation, while $\chi^{(3)}$ is responsible for third-harmonic generation, nonlinear refractive index and so on.

In the third-order nonlinear optical case, let us assume a monochromatic applied field given by

$$E(t) = E_0 \cos(\omega t). \tag{2.8}$$

As the third order nonlinear polarization is

$$P^{(3)}(t) = \varepsilon_0 \chi^{(3)} E^3(t). \tag{2.9}$$

by combining Eqs. 2.8 and 2.9 we have

$$P^{(3)}(t) = \frac{1}{4}\varepsilon_0 \chi^{(3)} E_0^3 \cos(3\omega t) + \frac{3}{4}\varepsilon_0 \chi^{(3)} E_0^3 \cos(\omega t), \tag{2.10}$$

where the identity

$$\cos^3(\omega t) = (1/4)\cos(3\omega t) + (3/4)\cos(\omega t) \tag{2.11}$$

was used.

The first term of Eq. 2.10 is related to the third-harmonic generation, as there is a response of frequency 3ω to an applied field with frequency ω [32], represented by Fig. 4. The second term indicates a nonlinear behavior at the same optical field frequency to the polarization, which leads to a nonlinear change to the refractive index, suffered by a wave at frequency ω [32]. This nonlinear contribution to the refractive index can be represented by

$$n' = n_0 + n_2 I, \tag{2.12}$$

where n_0 is the usual refractive index (linear case), I is the intensity of the incident beam,

$$I = \frac{1}{2} n_0 \varepsilon_0 c {E_0}^2, \tag{2.13}$$

and n_2 is the nonlinear refractive index, given by

$$n_2 = \frac{3}{2n_0^2\varepsilon_0 c}\chi^{(3)}. \quad (2.14)$$

This is the nonlinear optical Kerr effect: the refractive index of a given material varies according to the incident light wave intensity.

Figure 4 – Third-harmonic generation simplified diagram. The solid and dashed line represents the real and virtual energy levels, respectively.

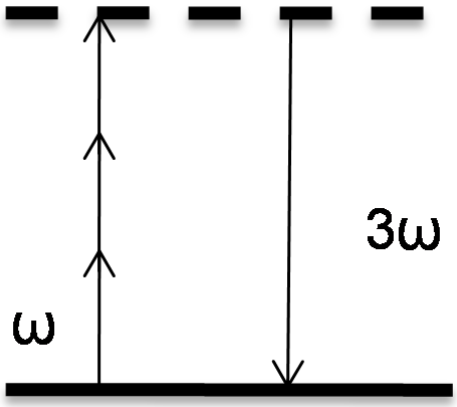

Source: by the author.

Among the nonlinear effects, there is the so-called nonlinear absorption. In non-metallic materials, the valence band (the highest occupied energy level) is separated by an energy gap (bandgap) from the conduction band (the lowest unoccupied energy level). Light can only be absorbed if the photon energy is greater than the bandgap (E_g), promoting electrons from the valence to the conduction band – that is the process of linear absorption[33], seen in Fig. 5, where VB and CB are the valence and conduction band respectively. Thus, in linear absorption

$$h\nu > E_g. \quad (2.15)$$

where E_g is the gap energy, h is the Plank's constant and ν is the light frequency.

Figure 5 – Linear absorption of light in a non-metallic material.

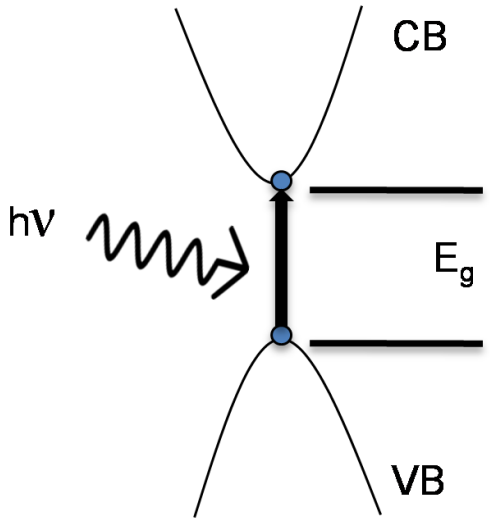

Source: by the author.

In cases where a single photon does not have enough energy to excite an electron through the energy gap ($h\nu < E_g$), absorption can only occur through nonlinear absorption processes: photoionization and avalanche ionization[33].

The first process can be split in two different cases, the tunneling and multiphoton ionization. In the first case, this process (Fig. 6(a)) occurs due to the applied electric field suppressing the potential that binds the valence electron, allowing it to become a free electron. In multiphoton ionization, a process associated to the imaginary portion of the nonlinear susceptibility[34], multiple photons are simultaneously absorbed by a single electron in the valence band. Thus, for an electron to be promoted to the conduction band by m photons,

$$mh\nu > E_g, \tag{2.16}$$

as seen on Fig. 6(b).

In the case of avalanche ionization, an electron already in the conduction band (called “seed” electron) absorbs multiple photons until it surpasses, by at least the gap energy, the conduction energy minimum. Then, by colliding with an electron from the valence band, it results in two electrons at the conduction band minimum (impact ionization), as seen in Fig. 6(c). This process repeats itself as long as the laser remains on the sample, promoting an exponential growth of electrons in

the conduction band, thus being named an avalanche process. The seed electron, necessary for the avalanche ionization, is usually originated by one of the previously discussed ionization processes during fs-laser pulses excitation.

Figure 6 – Nonlinear photoionization: (a) Tunneling ionization, (b) multiphoton ionization and (c) avalanche ionization.

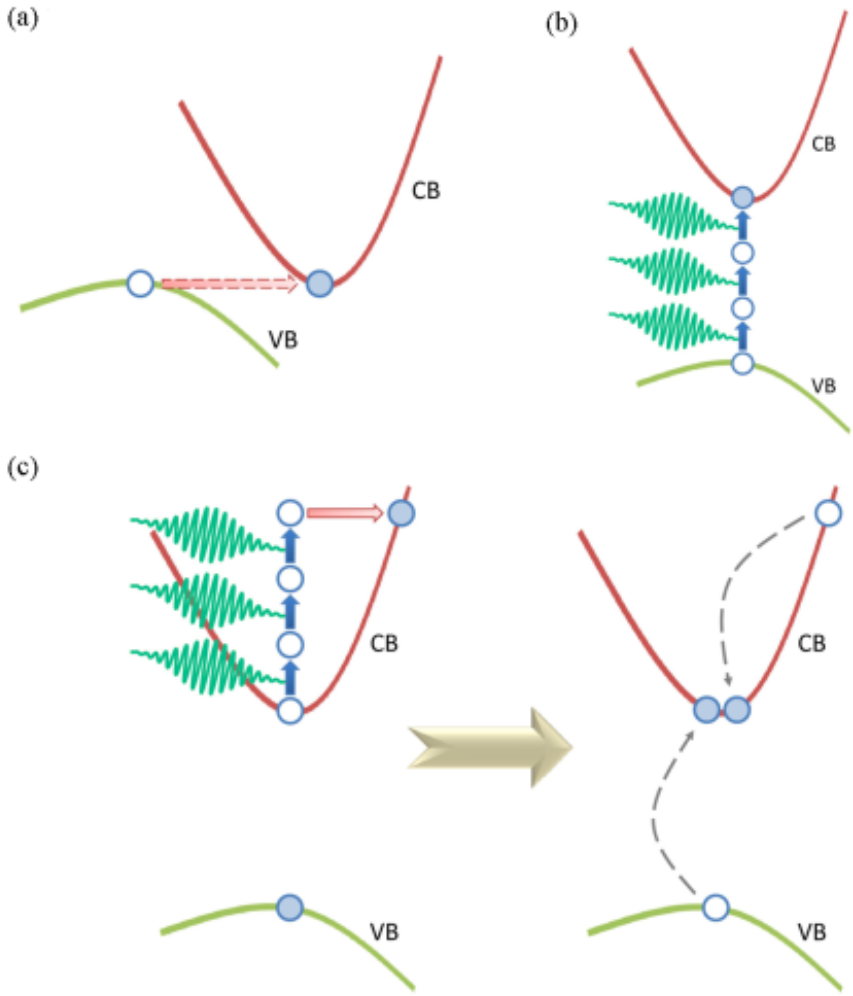

Source: adapted from Ams[33].

According to Keldysh[35], both tunneling and multiphoton ionization are the same effect, being distinguished by a low-frequency regime (where the tunneling effect is predominant) and a high-frequency one (associated to multiphoton ionization). This can be determined through the ratio of the tunneling time of an electron as compared to the period of the laser, the so called Keldysh parameter (γ_K), that can be alternatively given by the ratio of the tunneling and laser frequency,

$$\gamma_K = \frac{\nu}{e}\sqrt{\frac{m_e \varepsilon_0 c n_0 E_g}{I_0}}, \qquad (2.17)$$

where ν and I_0 are the laser light frequency and peak intensity, e and m_e are the electron's charge and mass, c is the light speed, and finally n_0 is the material's refractive index.

Figure 7 – Photoionization regimes according to Keldysh[35].

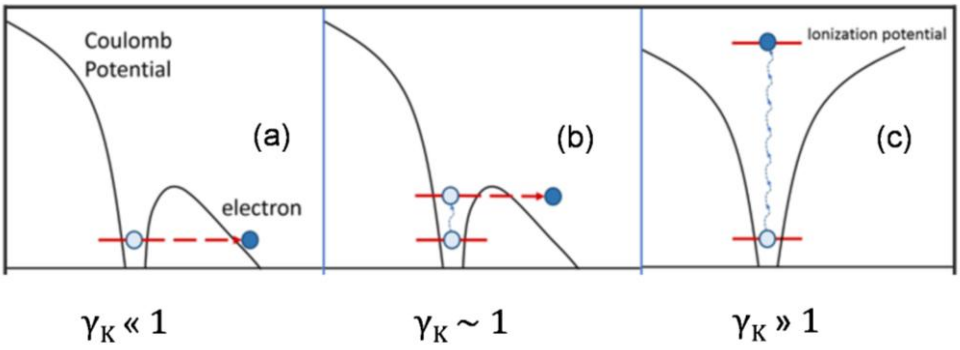

Source: adapted from Mery[36].

If $\gamma_K \ll 1$, it is in the low-frequency regime, indicating that it can be interpreted as if the optical field is a static one, suppressing the binding potential[35]. In other words, If $\gamma_K \ll 1$, tunneling ionization is the dominant process, as seen in Fig. 7(a). On the other hand, in the case where $\gamma_K \gg 1$, the electron is in a high-frequency regime, oscillating so quickly that it doesn't perceive the distortion in the potential, making multiphoton ionization more prevalent[35], seen in Fig. 7(c). Finally, if $\gamma_K \sim 1$, it is considered to be in a intermediate regime, where both multiphoton and tunneling ionization takes place simultaneously, seen in Fig. 7(b).

2.3. Femtosecond laser micromachining fundamentals

As discussed in previous sections, the femtosecond laser can generate extremely intense short pulses. Thus, it is able to achieve nonlinear ionization processes, causing the ionization of a large density of electrons. Such high number of electrons, once it gets to a certain critical density value, causes permanent lattice damage on the material, as this plasma formation continually absorbs the incident radiation – that is the so-called optical breakdown process[37]. This phenomenon was explored since the beginning of the laser invention, with laser damage in glass being

reported in 1964[38]. This prompted many studies in the field of light-matter interactions, when in 1995, sub-micrometric holes were generated in a metal film using a Ti:sapphire laser that generates ~100 fs pulses at 800 nm[39], paving the way for the femtosecond laser micromachining processing technique.

Fs-micromachining consists of producing micrometric structures with great precision in either the surface or bulk of a material. Such high spatial resolution is attributed to the nonlinear absorption processes, as they are dependent of the laser intensity. Thus, only at the laser focal volume does the material suffer damage by the femtosecond pulses. In addition, due to the fact that the femtosecond laser pulse duration is shorter than the ion's vibrational period, it results in most of the energy being transferred to the material electronic distribution, increasing the density number of free electrons and heating them, while the lattice remains "frozen" to the heat effects, according to the two-temperature model[1,40,41], resulting in a confined damage region. Figure 8 illustrates the damage confinement of an ultrashort pulse (b) compared to a longer one (a), where it can be noted that in the longer pulse duration case, heat effects are present.

Figure 8 – Comparison of the light-matter interaction of a laser with a long pulse (a) to ultrashort pulse duration (b).

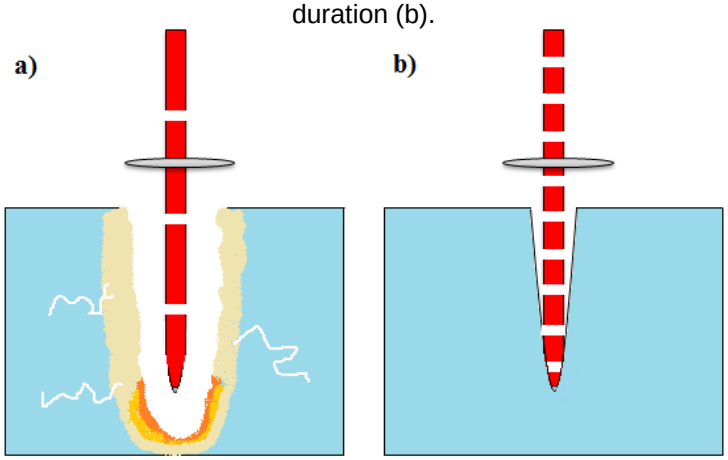

Source: by the author.

Once the electrons density reaches its critical point, it transfers its energy to the lattice, quickly heating it above its vaporization point, resulting in an abrupt phase explosion (adiabatic expansion)[42–44], removing material from the surface alongside the thermal energy. Simultaneously, as the fs-pulse laser excites the material, seed electrons are created, commencing the avalanche ionization process or being ejected from the material due to its excited state. This can lead to a

Coulomb explosion[45–47], once the surface charge becomes imbalanced. The conjunction of these fs-laser pulse surface damage outcomes is the ablation process.

During the processing of materials with femtosecond laser micromachining, the knowledge of the material's damage threshold fluence (the minimum applied energy per area required to produce damage) is of foremost importance, since laser operation near this value optimizes the micromachining resolution and, at the same time, minimizes collateral damage, as thinner lines are produced. This threshold value can vary since it depends on the presence of defects, dopants, impurities, among many other factors[48,49], either modifying local electronic density or creating intermediate levels in the bandgap, facilitating the ionization process.

As defects can be externally generated by fs-laser pulses, when multiple pulses are applied, a cumulative effect known as incubation can take place[50–52]: the damage threshold energy decreases the more pulses are applied per spot of the material. Thus, it is crucial that we take into account this effect in order to have complete information about the damage threshold fluence of a material.

3. EXPERIMENTAL

Chapter 3 addresses the experimental part of this dissertation, explaining the experimental setup in detail, the materials utilized as well as the methodology applied to study the micromachining process.

3.1. Experimental setup

The micromachining of the samples was carried out using a high repetition rate femtosecond laser system. It emits 216 fs pulses (at the laser exit), with its first harmonic output centered at 1030 nm, second harmonic at 515 nm and third at 343 nm. This fs-laser is based on a chirped pulse amplification (CPA) technique, which uses directly diode-pumped Yb:KGW as an active medium, and has its repetition rate controlled (from 1 MHz to ~100 Hz) via a Pockels cell-based pulse selector. The Pockels cell takes advantage of the Pockels effect: an applied electric field generates a linear change in the birefringence of a material, thus being able to change the polarization of an incoming light. The Pockels cell acts as a fast shutter, being able to select the number of incoming laser pulses.

The experimental setup consists of a microscope lens (NA = 0.65 objective) to focus the beam onto the sample, which is mounted on a three-dimension computer-controlled motorized translation stage (with micrometric precision), as seen in Fig. 9. The fs-micromachining can be seen through the use of a CCD camera, capturing the whole process in real-time.

Figure 9 – Simplified micromachining experimental setup.

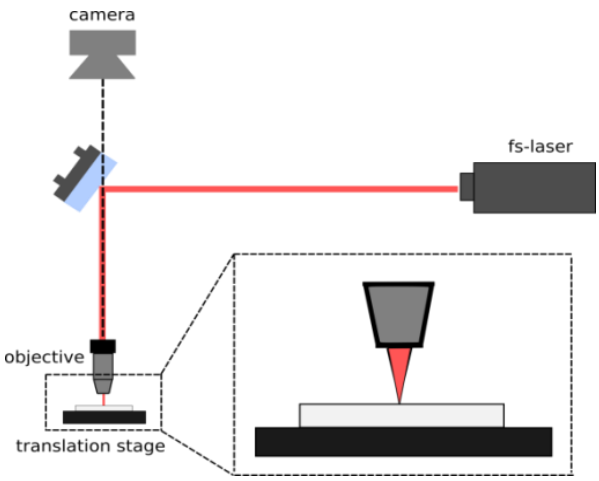

Source: by the author.

3.2. Zero damage method

The zero damage method[53] was utilized in order to evaluate the incubation effect of the GaN and CVD diamond samples. The method is based on utilizing Gaussian-intensity profiles with distinct energies to produce damage on the sample's surface. The higher the applied energy, the thicker the produced lines are, as seen in Fig. 10, which displays the straight micromachined grooves on the surface of the sample with the applied fluences (J/cm²) increasing from top to bottom at a fixed scanning speed (0.025 mm/s), produced by one hundred laser pulses per spot of the sample at 1030 nm.

Figure 10 – SEM image of micromachined lines with distinct fluences on the GaN film for one hundred pulses at 1030 nm.

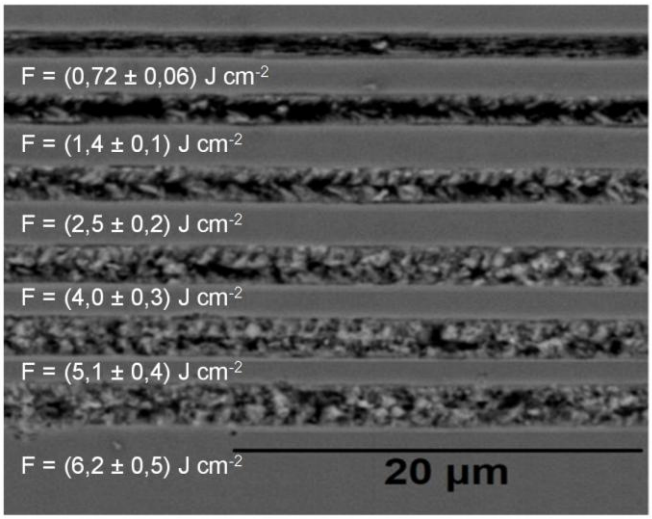

Source: by the author.

Given the intensity of an Gaussian pulse

$$I(r,t) = I_0 \exp\left(-\frac{r^2}{\rho^2}\right) \exp\left(-\frac{t^2}{\tau^2}\right), \tag{3.1}$$

where I_0 is the peak intensity, and ρ and τ are the spatial and temporal radii at the $1/e$ intensity contour, its fluence (J/cm²) can be obtained by integrating Eq. 3.1 in time, resulting in

$$F(r) = F_0 \exp\left(-\frac{r^2}{\rho^2}\right), \tag{3.2}$$

where $F_0 = \sqrt{\pi}\tau I_0$ is the peak fluence at the center of the beam. Thus, if this pulse is focused on a sample surface, it will generate a circular pattern that is associated with a radius r_{th} and fluence F_{th}, given by

$$r_{th}^2 = \rho^2 \ln\left(\frac{F_0}{F_{th}}\right), \tag{3.3}$$

which can be alternatively described as

$$r_{th}^2 = \left(\frac{w_0^2}{2}\right) \ln\left(\frac{E_p}{E_{th}}\right), \tag{3.4}$$

where $\rho^2 = w_0^2/2$, w_0 is the Gaussian beam waist at the focus region, E_{th} is the threshold energy and E_p is the pulse energy, that is related to the peak fluence by

$$E_p = F_0 \pi \rho^2. \tag{3.5}$$

Thus, with the characterization of the fs-pulse damage on the surface of the material given by Eq. 3.4, we can determine the fluence threshold (F_{th}), defined as

$$F_{th} = (2E_{th})/[\pi (w_0)^2], \tag{3.6}$$

by measuring the modified area dimensions, via Scanning Electron Microscopy (SEM) or optical microscopy (ZEISS LSM – 700) and plotting its squared radius (r_{th}^2) as a function of the pulse energy (E_p), defined as

$$E_p = \bar{p}/f\ , \tag{3.7}$$

where $\bar{p}$ is the average power of the laser beam, measured by a power meter, and f is the fs-laser repetition rate.

3.3. Materials

3.3.1. Gallium nitride (GaN)

Gallium nitride (GaN), known for its wide band gap of 3.4 eV at room temperature is one of today's most relevant materials in optoelectronics, given its stability in high temperatures, high thermal conductivity, large electrical breakdown field, high field electron velocity and mobility[54] as well as a wide transparency window, shown in Fig. 10, where the energy gap can also be noted from the absorbance peak at ~364 nm (3.4 eV). The oscillating pattern seen in the absorbance graph occurs due to Fabry-Perot interference as the GaN sample is a thin film, acting as two parallel surfaces by which light can be reflected/transmitted and interfere with each other. Thus, it is used in the manufacture of LEDs[55], high-temperature electronic devices[56] and field-effect transistors (FETs)[57,58], a transistor that controls the flow of current through an electric field. GaN also has been demonstrated to have interesting nonlinear optical proprieties, such as second harmonic generation[59], and nonlinear refractive index below the band gap[60], being relevant on the field of photonic devices as well. It possesses the wurtzite crystal structure, seen in Fig. 12, where the yellow spheres represent Ga and the gray ones N.

Figure 11 – Absorbance as function of the excitation wavelength of the GaN sample.

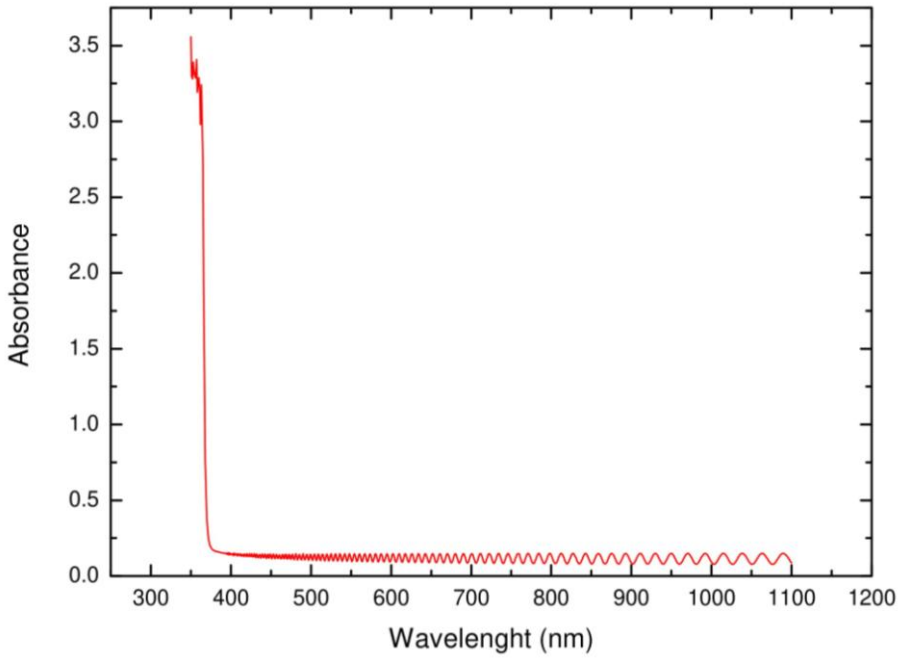

Source: by the author.

The experiment was carried out on a GaN thin film, provided by Prof. T. Voss of the Institute of Semiconductor Technology and Laboratory for Emerging Nanometrology LENA, Technische Universität Braunschweig, Brunswick, Germany. The sample was grown through epitaxy (a procedure where the deposited film's crystalline orientation is influenced by the crystalline orientation of the substrate[61]) in an Aixtron AIX2600G3 HT MOVPE reactor on a 650 µm thick, double-side-polished 10 cm sapphire substrate. Following a standard procedure for GaN growth, the bare sapphire substrate was thermally cleaned in a H_2 atmosphere. Afterwards, a GaN nucleation layer was deposited using trimethylgallium (TMGa) and ammonia (NH_3) at low temperature prior to a high temperature recrystallization step. A 9.3 µm thick GaN buffer layer was subsequently grown with a TMGa supply of 1mmol/min and V/III ratio of 550 at a temperature of 1050 ºC and a reactor pressure of 290 mbar under H_2carrier gas. Silane doping was employed, resulting in an n-type donor concentration of 3×10^{17} cm^{-3}.

Figure 12 – GaN wurtzite crystal structure: the yellow spheres represent Ga while the grey spheres N.

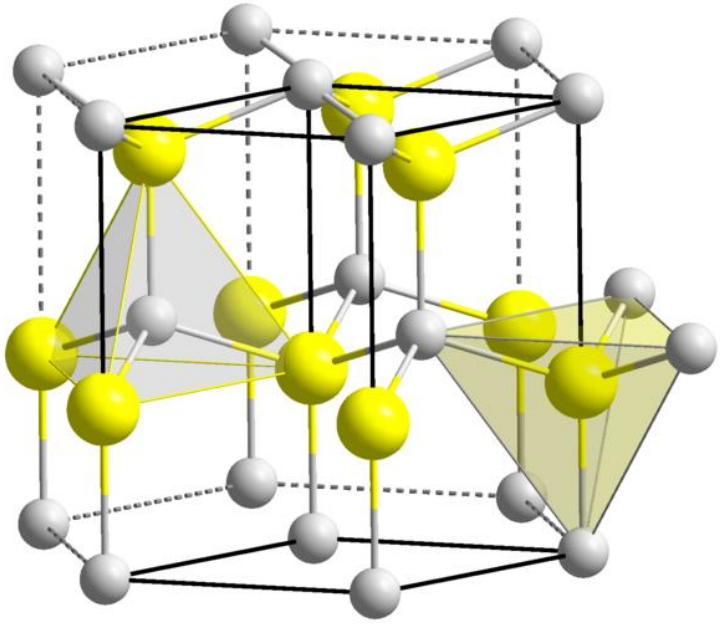

Source: adapted from Hill[62].

3.3.2. CVD diamond

Diamond is a wide bandgap semiconductor (E_g = 5.47 eV), famous for

its extraordinary proprieties such as its hardness (highly explored in mechanical applications), its optical proprieties (transparent from UV up to the microwave region, shown partially in Fig. 13, where the gap energy can also be noted at the absorbance peak at ~226 nm, e.g. 5.47 eV),it possesses a refractive index of 2.4, low thermal expansion coefficient, high thermal conductivity, high breakdown voltage and high carrier mobility[63,64], being a highly sought after material for on-chip photonics[65]. Diamond is also known to host many different color centers, which are defects associated with trapped electrons or holes[66], that can be generated externally. Those defects are currently being studied for applications in quantum photonics, as they could be explored as quantum emitters of light and optically accessible qubits[67].

Figure 13 – Absorbance as function of the excitation wavelength of the CVD diamond sample.

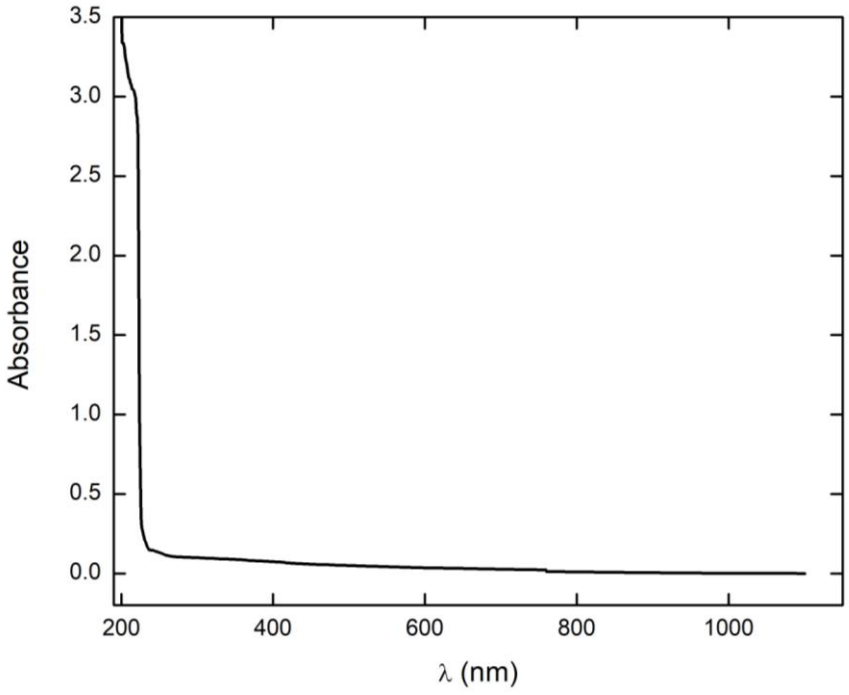

Source: by the author.

Its crystal structure is a variation of the zinc blende, where carbon atoms occupy all available positions, with each carbon covalently bonded with four others, forming the diamond cubic crystal structure[68], seen on Fig. 14. In order for it to have a practical commercial use, many techniques were proposed for its synthetic production, one of which being the chemical vapor deposition (CVD) method, enabling a better control over the desired proprieties. Much like GaN, CVD diamond also possesses reported nonlinear optical proprieties, such as stimulated Raman scattering generation[69] and two and three-photon absorption[70].

Figure 14 – Diamond crystal structure.

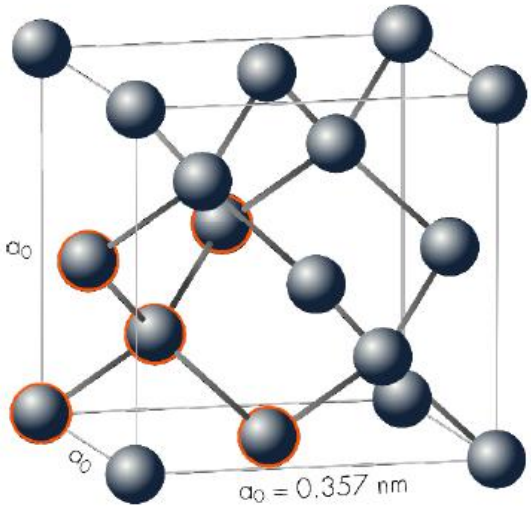

Source: adapted from Element Six™ [71].

The chemical vapor deposition (CVD) technique (Fig. 15) consists essentially of the heating, with a temperature above 2000 ºC, of hydrogen and a gaseous source of carbon (usually methane) which becomes plasma. There are many ways of heating the plasma phase: radiofrequency, laser induced, direct current, hot filament, chemical reaction and finally microwaves. The CVD diamond is then deposited in a substrate and its formation relies on the fact that under certain conditions with the presence of atomic hydrogen, the formation of diamond is more favorable than of the graphite (having a faster nucleation and growth rate)[71,72].

Figure 15 – Chemical vapor deposition simplified experimental setup.

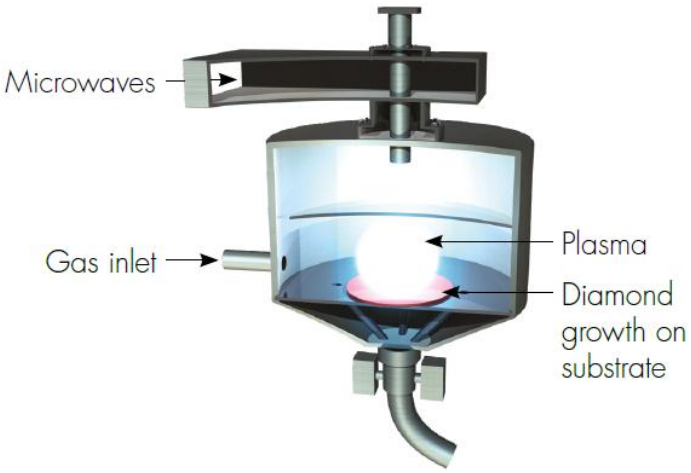

Source: adapted from Element Six™ [71].

In this work, we employed a single crystal CVD diamond (2.5 x 2.5 x 0.3 mm) produced by Element Six^{TM} with a boron and nitrogen impurity lower than 1 ppm, seen in divisions 1 and 3 of Fig. 16.

Figure 16 – CVD diamond samples seen in divisions 1 and 3.

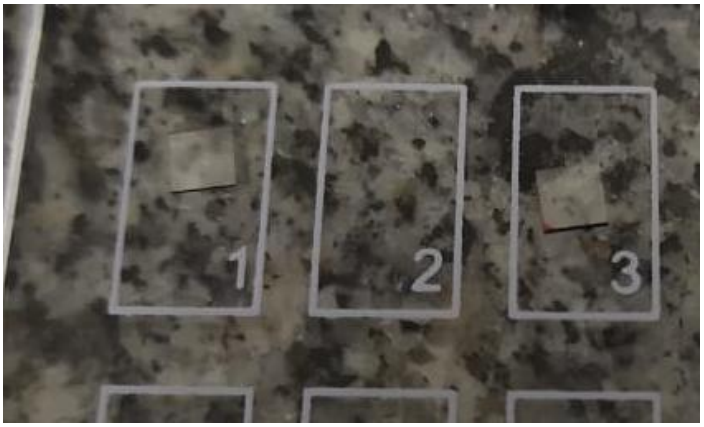

Source: by the author.

4. RESULTS

In this chapter, we will report our experimental results of the fs-pulse micromachining of GaN and CVD diamond, and a comparison with a theoretical model to validate the results and further understand the fs-laser pulse processing technique.

4.1. Gallium Nitride

The damage threshold fluence of GaN for a specific number N of pulse superposition was determined for all three wavelengths (343 nm, 515 nm and 1030 nm) utilizing the method described in section 3.2.

The number of pulses per spot (N) was controlled by scanning the sample at different speeds (V) and pulse's repetition rate (f), since it is calculated by taking the ratio between the summation of the intensities generated by fs-pulses in a single spot, and the intensity of a single pulse centered in that point[21,73]. This summation can be perceived as a Jacobi theta function[74] (ϑ_3), given by

$$N = \vartheta_3\left(0, e^{-2\left(\frac{V}{fw_0}\right)^2}\right) \tag{4.1}$$

that can be simplified in the case for a large amount of pulse superposition to

$$N = \sqrt{\pi/2}(fw_0)/V \approx 1.25 fw_0/V, \tag{4.2}$$

as the ratio $(V/fw_0) \approx 0$, since it would require a low scanning speed or high laser frequency.

Thus, we obtained the damage threshold fluence for 1 to about 10^5 pulses per spot of the GaN sample, with the combination of Eq. 4.1 and the zero damage method. Figure 17 displays one example of the many graphs necessary for the study of the incubation effect. It reveals the relationship between the squared half-width of the micromachined lines as a function of the pulse energy, correctly predicted by Eq. 3.4, used as the fitting (dashed line) for about one hundred 1030 nm pulse superposition on the GaN sample, from which we determined the minimal laser fluence to produce damage to be as (0.13 ± 0.05) J/cm^2 and the Gaussian beam

waist at the focus w_0 = (1.2 ± 0.1) µm.

Figure 17 – Squared half-width of micromachined lines as function of the pulse energy of GaN for about one hundred 1030 nm pulses.

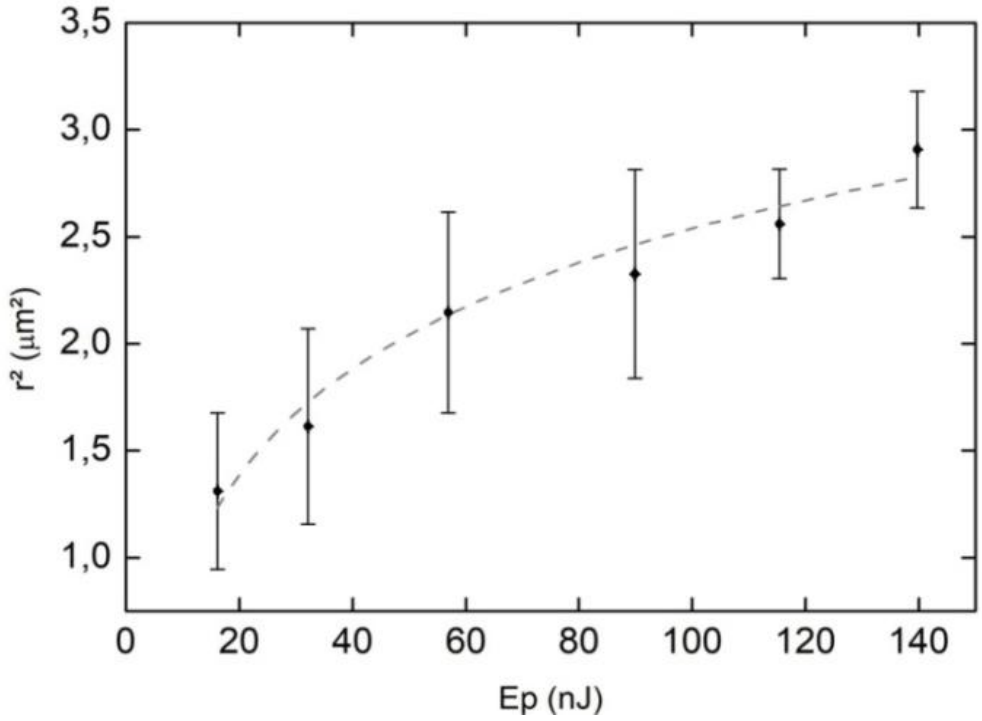

Source: by the author.

The cumulative behavior of the incubation effect can be studied through a graph of the damage threshold fluence as a function of pulse superposition, determined by the previous steps, as seen in Figs. 18-20 for 1030 nm, 515 nm and 343 nm, respectively.

Many models have been proposed to describe this effect[51,75], from a more simple empirical ansatz such as

$$F_{th,N} = F_1 N^{S-1}, \tag{4.3}$$

where $F_{th,N}$ is the fluence for a N pulse superposition, F_1 is the fluence of a single pulse, and S is a free parameter, to a more complex one that takes into account the saturation of induced effects that can occur for a large number of pulses, given by

$$F_{th,N} = \left(F_{th,1} - F_{th,\infty}\right)e^{-k(N-1)} + F_{th,\infty}, \tag{4.4}$$

where $F_{th,\infty}$ and $F_{th,1}$ are the infinite and single pulse ablation threshold fluence and k

is an empirical constant named incubation parameter. This parameter describes the efficiency of the cumulative effect: the higher its value, the fewer pulses are required to reach the minimum damage threshold fluence ($F_{th,\infty}$), on the bottom plateau of an incubation effect graph.

In Fig. 18 we present the results of the incubation cumulative effect during the fs-micromachining of the GaN sample using 216 fs pulses at 1030 nm, a three-photon absorption mechanism, with $F_{th,N}$ in function of the number of pulse superposition N. The dashed gray line corresponds to Eq. 4.4, which correctly describes the experimental behavior of the $F_{th,N}$ saturation for the high-pulse superposition region. From this graph, we can observe a sizable decrease from (0.67 ± 0.07) J/cm² to a mean value of (0.10 ± 0.02) J/cm² in about one hundred pulses per spot of the sample. Such behavior is attributed to the cumulative defects generated by the fs-pulses before the ablation process takes place. With the increase in the number of pulses interacting with the GaN sample, the number of defects is greater, facilitating the optical damage process as this could lead to a modification on the local electronic density or the creation of sub-bandgap energy levels, accelerating the ionization process.

Figure 18 – Damage threshold fluence as function of pulse superposition of GaN with 1030 nm laser pulses.

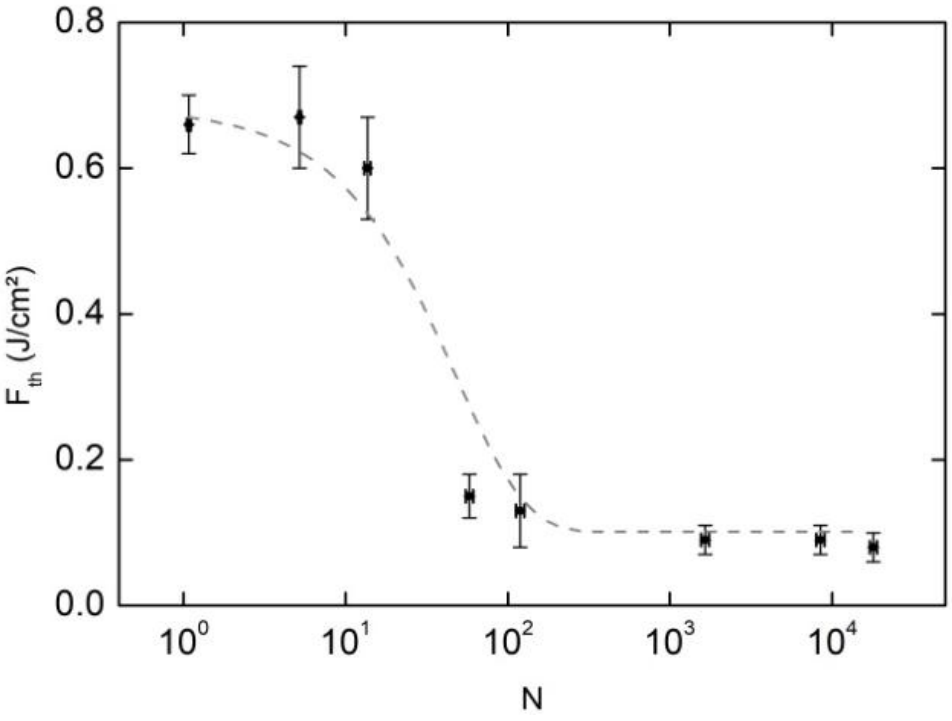

Source: by the author.

Figure 19 displays the incubation effect of GaN under the excitation of 216 fs pulses at 515 nm, a two-photon absorption process, through a graph of the damage threshold fluence in function of the number of fs-pulses per spot, determined by the combination of the zero damage method and Eq. 4.1 and 4.2, with the experimental data fitted by Eq. 4.4. Much like Fig. 18, this graph presents a decrease of $F_{th,N}$ from (0.21 ± 0.01) J/cm² to a mean value of (0.037 ± 0.002) J/cm² in about one hundred pulse superposition number. Again, this behavior is very well described by the incubation cumulative effect: with the increase of the fs-pulse per spot interaction with the sample, there is an increase in the defect generation, which directly leads to a facilitation of the optical damage process. In contrast to the 1030 nm excitation case, the values of the damage thresholds are considerably lower, which could be attributed to the difference of the absorption process: from three to two-photon absorption at 515 nm.

Figure 19 – Damage threshold fluence as function of pulse superposition of GaN with 515 nm laser pulses.

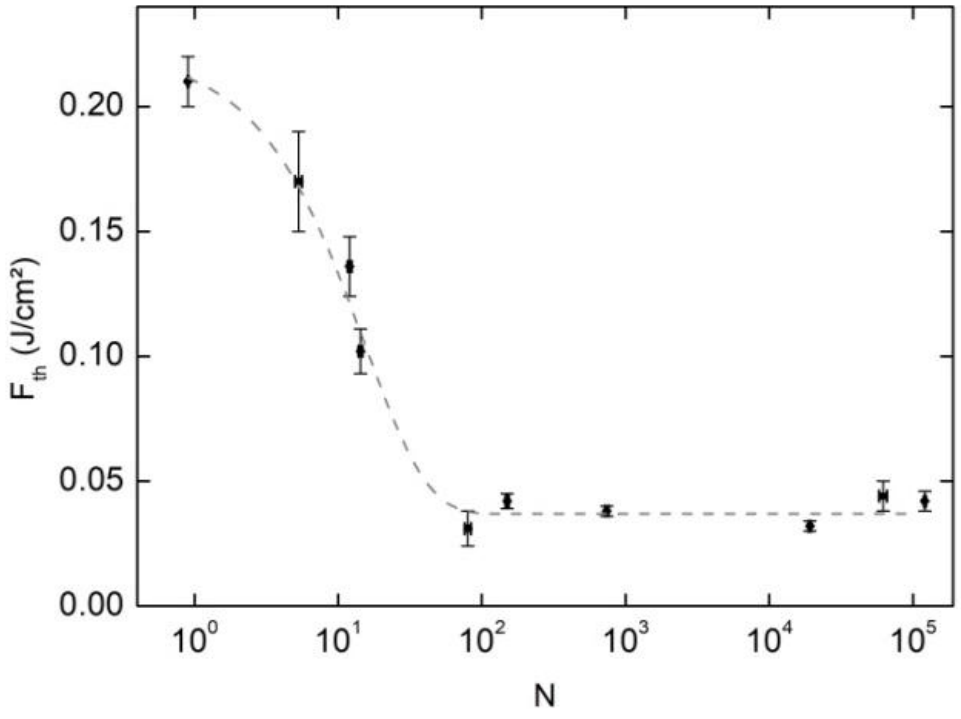

Source: by the author.

Figure 20 illustrates the incubation cumulative effect of GaN for 216 fs pulses at 343 nm, a linear absorption or a 1-photon absorption process. The graph of the $F_{th,N}$ in function of the number of pulses per spot was determined trough the

same way as the previous cases (515 and 1030 nm): the fluence threshold was determined by a graph of the squared half-width of the micromachined grooves in function of the pulse energy, and the number of pulses by Eq. 4.1 and 4.2. As the number of pulses was increased, the damage threshold fluence decreased, in agreement to the incubation effect, from (0.12 ± 0.01) J/cm² to (0.060 ± 0.003) J/cm² in ~10 pulse superposition number. The threshold fluence values presented on Fig. 20 are even lower than the ones determined at Fig. 18 and 19 at 1030 nm and 515 nm, which is the expected behavior, since this is a linear absorption process.

Figure 20 – Damage threshold fluence as function of pulse superposition of GaN with 343 nm laser pulses.

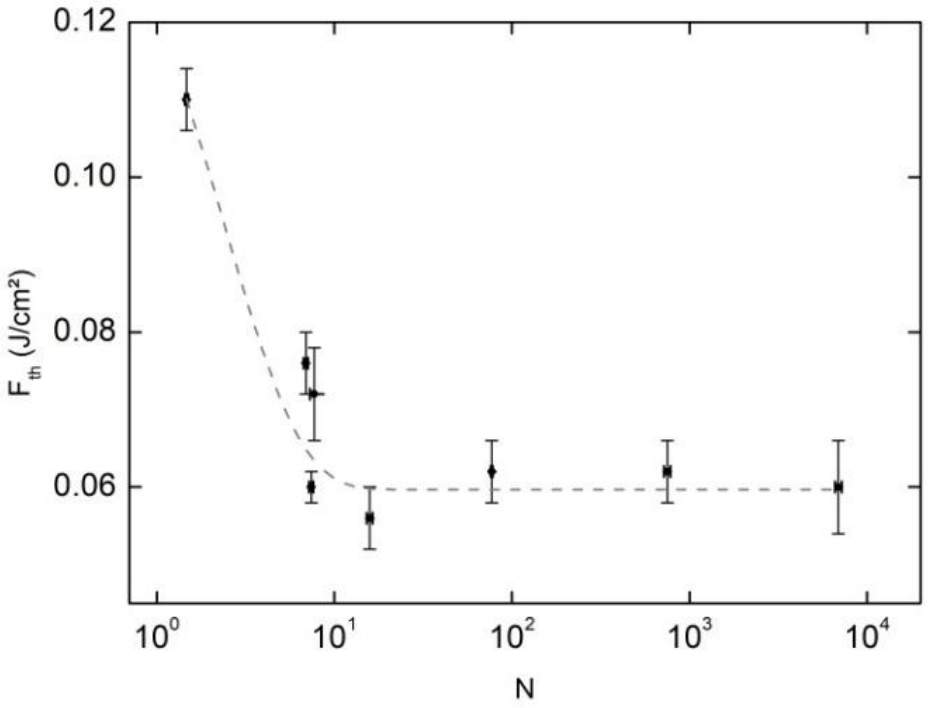

Source: by the author.

The region from N = 1 to ~100 shows a drastic decrease in the threshold fluence for the IR and green wavelengths (1030 and 515 nm), from (0.67 ± 0.07) J/cm² to a mean value of (0.10 ± 0.02) J/cm² for the 1030 nm case, and from (0.21 ± 0.01) J/cm² to a mean value of (0.037 ± 0.002) J/cm² for the 515 nm case, which remains constant with the increase of pulses per spot in both cases. The 343 nm case, on the other hand, has a much faster decrease in threshold fluence when compared to the previous ones: from (0.12 ± 0.01) J/cm² to (0.060 ± 0.003) J/cm² in ~10 pulses per spot. This phenomenon can be further explored in the graph of the incubation parameter as a function of the fs-pulse wavelength in Fig. 21, as even

though the discrepancy in the error is high (the error is associated to the fitting of the incubation curves by Eq. 4.4), it shows that it decreases as we increase the applied fs-pulse wavelength: k = (0.4 ± 0.1) at 343 nm, k = (0.07 ± 0.01) at 515 nm and k = (0.02 ± 0.01) at 1030 nm. Thus, the cumulative incubation effect is more efficient at 343 nm, followed by the 515 and 1030 nm cases, according to the definition of the incubation parameter given by the exponential defect accumulation model. As mentioned before, the multiphoton absorption processes present during the femtosecond micromachining of the GaN sample at 343 nm, 515 nm and 1030 nm are the one-photon absorption (linear absorption), followed by the two and three-photon absorption effects respectively. This inversely proportional behavior of k and λ could be directaly related to those processes, as the linear absorption is much more probable to occur than the two and three-photon absorption, requiring less pulses to reach the defect saturation region defined by the $F_{th,\infty}$ value.

Figure 21 – Incubation parameter *k* obtained from the incubation curves of GaN as function of the applied wavelength linked by a guideline (black line).

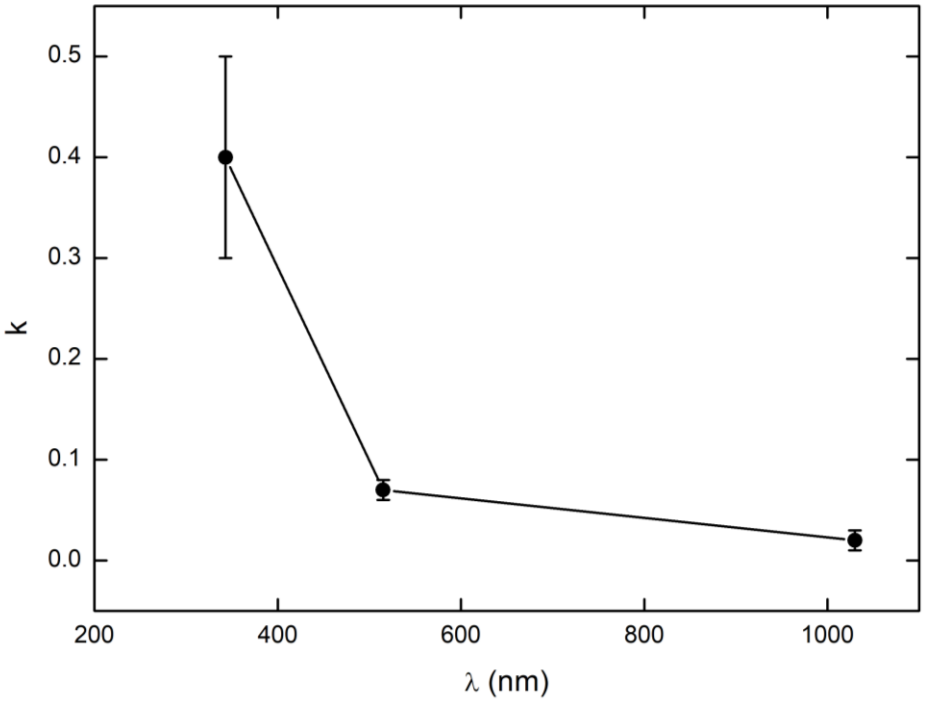

Source: by the author.

As a means of comparison and to further investigate the fs-micromachining process, we utilized a theoretical model to determine the single pulse damage threshold[76]. It takes into account the fact that through nonlinear ionization processes such as multiphoton and avalanche ionization, there is a

formation of an electron density that when it reaches a certain value, damage takes place on the surface of the material. The model assumes that the process of multiphoton and avalanche ionization (both present during micromachining) can be separated. Thus, the single pulse fluence given by

$$F_{th,1} = \frac{I_0 \tau}{2}\left(\frac{\pi}{ln\,2}\right)^{1/2}, \tag{4.5}$$

where τ is the pulse duration and I_0 is the Gaussian pulse peak intensity can be determined.

According to the model, the produced electron number density (n) of a single pulse can be determined by

$$n = \sigma_m \left(\frac{\lambda}{hc}\right)^m \frac{N_s I_0^m \tau}{2}\left(\frac{\pi}{mln\,2}\right)^{1/2} exp\left[\frac{\alpha I_0 \tau}{4}\left(\frac{\pi}{ln\,2}\right)^{1/2}\right], \tag{4.6}$$

which can be simplified as

$$n = n_0 exp\left[\frac{\alpha}{2} F_{th,1}\right], \tag{4.7}$$

where n_0 is the total density of electrons produced by multiphoton ionization, m is the number of photons of the multiphoton ionization process, N_s is the solid atom density, σ_m is the m-photon cross-section and $2/\alpha$ is the scale fluence – that is, the value that determines the significance of the avalanche ionization, represented by the exponential in Eqs. 4.6 and 4.7, according to Stuart[76]. As an example, given a value of $2/\alpha$ = 0.2 J/cm² [76], if $F_{th,1}$ is on this order of magnitude, avalanche ionization is not of significance; if $F_{th,1}$ is below the scale fluence, photoionization is mostly responsible for the optical breakdown.

Finally, we can use Eq. 4.6 to determine the value of I_0 in order to calculate the threshold fluence of a single pulse, given by Eq. 4.5. This can be accomplished by a numerical simulation of n as a function of I_0 for m = 1, 2 and 3 since the GaN's energy gap is 3.4 eV and we are applying pulses of 343 (3.6 eV), 515 (2.4 eV) and 1030 nm (1.2 eV), as seen on Fig. 22. As explained in section 2.2, the transition of an electron is only possible when it is excited with energy greater than the bandgap, thus, the transition of an electron from the valence band (VB) to

the conduction band (CB), represented by the gray rectangles, is proportioned by the absorption of one (a), two (b) and three photons (c), illustrated as the straight arrows with sizes proportional to the amount of the photon energy (eV).

Figure 22 – One-photon absorption for 343 nm (a), two-photon absorption for 515 nm (b) and three-photon absorption for 1030 nm (c), considering bandgap (energy gap between the valence band, VB, and conduction band, CB) of 3.4 eV for the GaN.

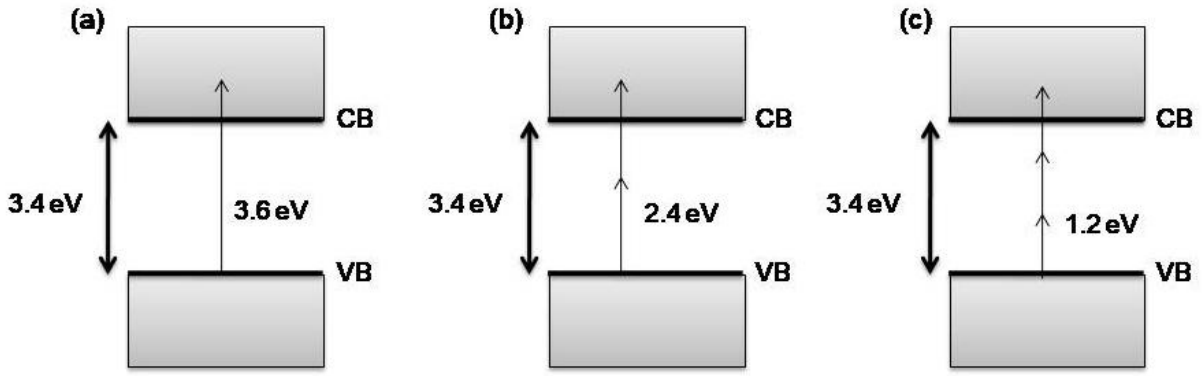

Source: by the author.

The simulations can be seen in Figs. 23-25 where the blue line represents the electron density n function given by Eq. 4.6 and the red dashed lines are the function's associated error. We, then, find the peak intensity for which $n = n_{cr}$, where n_{cr} is the critical electron density when material damage takes place upon excitation. The value for n_{cr} was adjusted to better fit the experimental data for m = 1 (one-photon absorption) case at 343 nm, resulting in the value of 2×10^{27} electrons/m^3, which was maintained for the m = 2 (two-photon absorption) and 3 (three-photon absorption) cases for consistency. From such intensity, the damage fluence threshold for a single pulse ($F_{th,1}$) is determined using Eq. 4.5 for each case.

The value of the solid atom density (N_s) was determined through

$$N_s = \frac{dN_A}{M}, \tag{4.8}$$

where d is the density of the material (g/cm³), N_A is the Avogadro's number, and M is the molecular mass (g/mol). As we are modeling the GaN sample, d = 6.15 g/cm³ at 300 K [77] and M = 83.73 g/mol, thus N_s = 4.42×10^{28} m^{-3}.

The absorption cross-section (σ_m) is determined by

$$\sigma_m = \frac{\alpha_m}{N_s}\left(\frac{hc}{\lambda}\right)^{m-1} \quad (4.9)$$

where α_m is the m-photon absorption coefficient, h is Planck's constant, c is the speed of light, and λ is the excitation wavelength.

In the first case at 343 nm, it is a linear absorption since $m = 1$. Thus it is only necessary to determine the linear absorption coefficient (α_1), which was found trough Beer Lambert's Law, given by

$$A = \log 10(e^{\alpha_1 L}), \quad (4.10)$$

where A is the absorbance and L is the optical path (GaN sample thickness). Eq. 4.10 can be alternatively described as

$$A = \log 10(1/T), \quad (4.11)$$

where the transmittance T is defined as

$$T = \frac{P_{out}}{P_{in}}, \quad (4.12)$$

and P_{in} and P_{out} are the femtosecond laser potency before and after passing through the GaN sample respectively. Thus, the linear absorption cross-section at 343 nm was determined to be σ_1 = (1.18 ± 0.05) ×10^{-23} m^2, through the use of Eq. 4.9.

As such, Fig. 23 shows the graph of the electron density n generated by the multiphoton and avalanche ionization processes on the GaN sample as a function of the peak laser intensity, I_0, at 343 nm by employing Eq. 4.6, calculating n in a determined range of intensities, so that the parameter n_{cr} = 2×10^{27} electrons/m³ can be seen. In this case, n was calculated from I_0 = 1×10^{15} W/m² up to I_0 = 8×10^{15} W/m². The error associated to the electron density is represented by the red dashed lines. They originated from the absorption cross-section coefficient determination given by Eq. 4.9 and were added/subtracted to the value of n. From the graph, in order to determine the value of the single-pulse damage threshold fluence given by Eq. 4.5, we must find the value of I_0 for which n_{cr} = 2×10^{27} electrons/m³, illustrated by the encounter of the black dashed lines. Thus, I_0 = (5.3 ± 0.4) ×10^{15} W/m² and

$F_{th,1}$ = (0.12 ± 0.01) J/cm², an exact replication of the experimental value of the single pulse threshold fluence, as the n_{cr} parameter was adjusted for this purpose.

Figure 23 – Electron density as function of the Gaussian peak intensity of GaN at λ = 343 nm, Ns = 4.42×10^{28} m^{-3}, σ_1 = (1.18 ± 0.05) ×10^{-23} m^2 and α = 10^{-23} m²/J [76]. The dashed red lines represent the curve associated error.

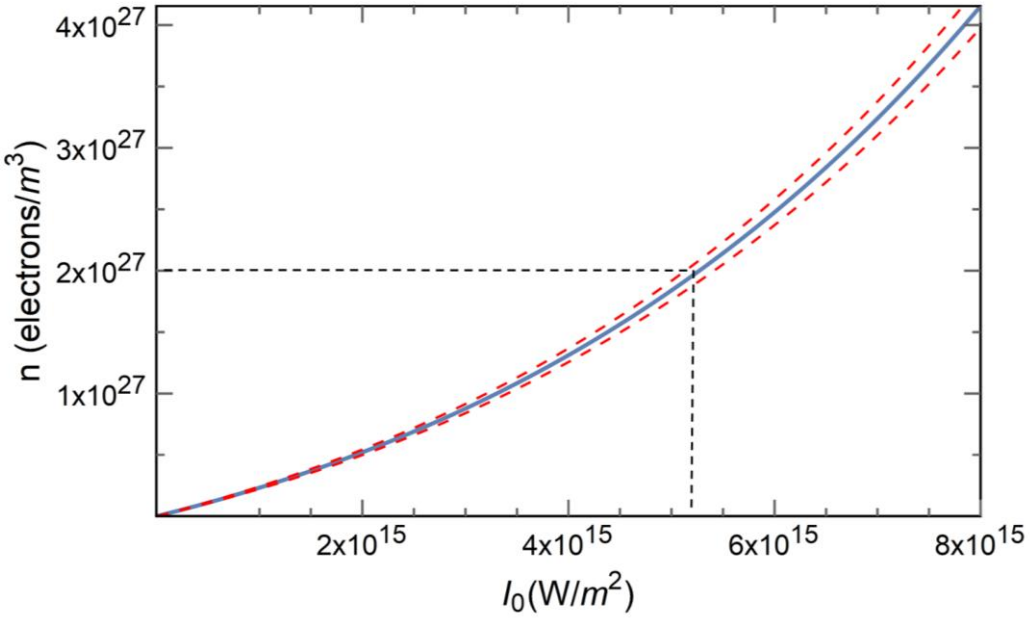

Source: by the author.

Figure 24 presents the numerical simulation of the generated density of electrons n in function of the peak laser intensity I_0 for 216 fs pulses at 515 nm – a two-photon absorption process. Much like the previous case, the density of electrons was calculated in a range of I_0 = 1×10^{15} W/m² up to I_0 = 1×10^{16} W/m² in order to observe the $n = n_{cr}$ moment. As it is caused by a nonlinear absorption process, the absorption cross-section was not calculated in the same way as the linear case trough Eqs. 4.10-12. Instead, we utilized Eq. 4.9 with an experimentally determined two-photon absorption coefficient at 515 nm for GaN[78], resulting in a two-photon cross-section of σ_2 = (2.4 ± 0.5) ×10^{-58} m^{4}s^{1}photon^{-1}. Thus, the I_0 for which n = 2×10^{27} electrons/m³ was determined to be I_0 = (8 ± 1) ×10^{15} W/m², resulting in a threshold fluence of $F_{th,1}$ = (0.18 ± 0.02) J/cm² at 515 nm, an equivalent result to the experimentally determined value of $F_{th,1}$ = (0.21 ± 0.01) J/cm². Like the 343 nm case, the error associated to the electron density, represented by the red dashed lines, is related to the absorption cross-section.

Figure 24 – Electron density as function of the Gaussian peak intensity of GaN at λ = 515 nm, Ns = 4.42×10^{28} m^{-3} , σ_2 = (2.4 ± 0.5) ×10^{-58} m^{4}s^{1}photon^{-1} [78] and α = 10^{-23} m²/J [76]. The dashed red lines represent the curve associated error.

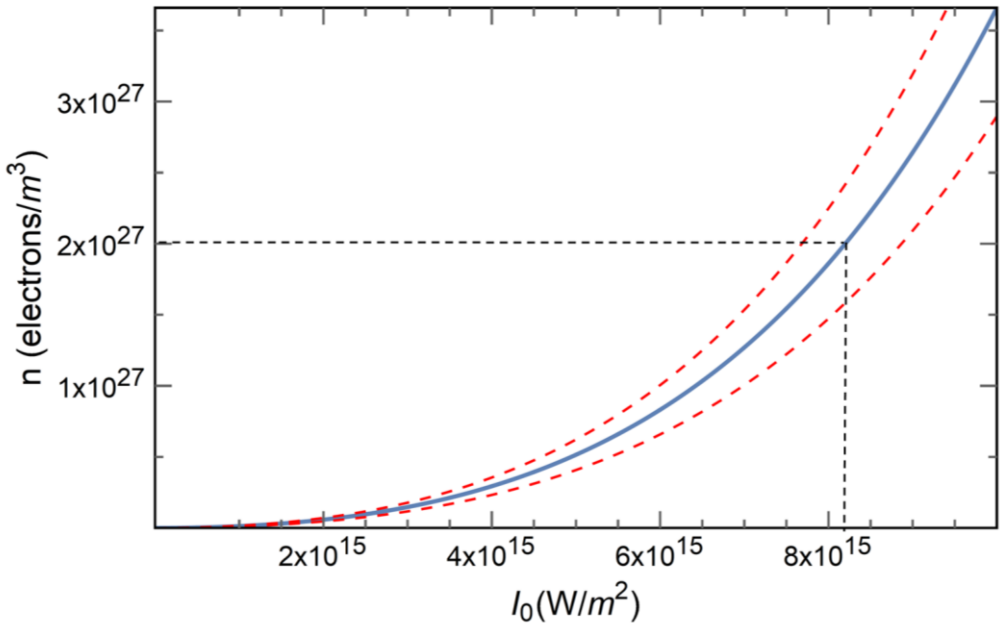

Source: by the author.

Lastly, in Fig. 25 we present the simulated electron density as a function of the laser peak intensity at 1030 nm – a three-photon absorption process, with I_0 varying from I_0 = 1×10^{15} W/m² up to I_0 = 2 ×10^{16} W/m².

Figure 25 – Electron density as function of the Gaussian peak intensity of GaN at λ = 1030 nm, Ns = 4.42×10^{28} m^{-3} , σ_3 = (8 ± 4) ×10^{-94} m^{6}s^{2}photon^{-2} from ZnO[79] and α = 10^{-23} m²/J [76]. The dashed red lines represent the curve associated error.

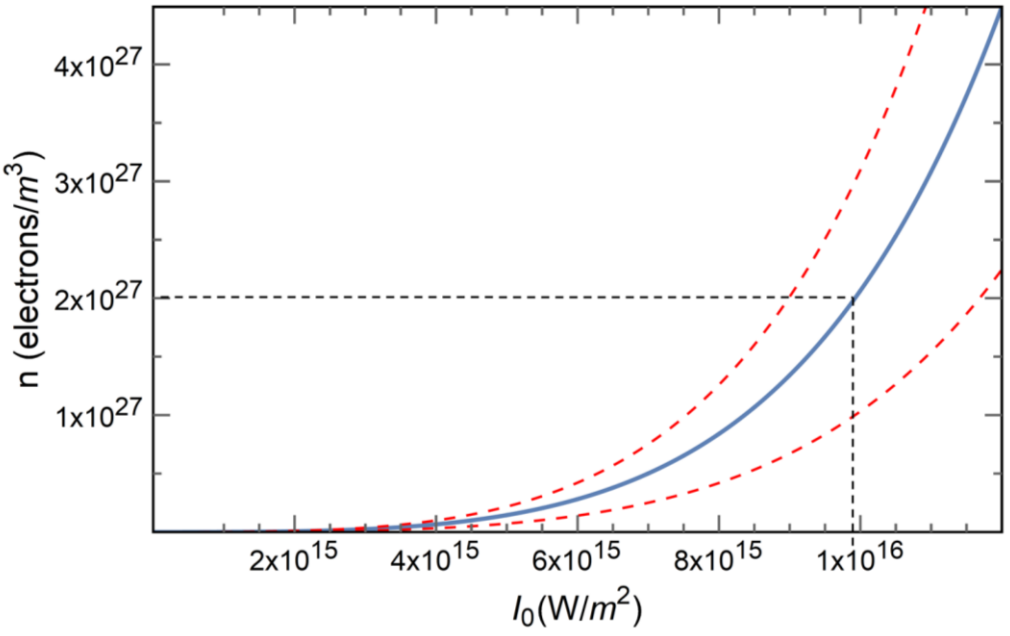

Source: by the author.

As it is a 3 PA process, its absorption cross-section was initially estimated using a typical three-photon absorption coefficient from a ZnO sample[79] using Eq. 4.9, as it was not found for GaN in the literature. However, as ZnO is also an semiconductor with the same crystal structure and similar bandgap (~ 3.3 eV [79]), it should be a good substitute. Thus, the 3 PA cross-section was determined to be σ_3 = (8 ± 4) $\times 10^{-94}$ $m^6 s^2 photon^{-2}$. Finally, the single pulse damage threshold can be determined to be $F_{th,1}$ = (0.23 ± 0.07) J/cm², as the I_0 for which $n = n_{cr}$ was found to be I_0 = (1.0 ± 0.3) $\times 10^{16}$ W/m². The noticeable increase of the error (red dashed lines) is related to the increase in the uncertainty of the m-photon absorption coefficient.

Figure 26 displays the experimentally determined $F_{th,1}$ (black circles), as well as the values obtained from the model (gray squares) as function of the excitation wavelength. The modeled values agree with the experimental data at 343 nm (one-photon) and 515 m (two-photons). However, the value from the model does not match the experimental result at 1030 nm (three-photons) using a typical three-photon absorption cross-section value[79]. In fact, in order to describe the experimental result at 1030 nm (0.67 J/cm^2) a three-photon absorption cross-section about 200 times smaller needs to be used (blue triangle).

Figure 26 – Damage threshold fluence of GaN for a single pulse in function of the excitation wavelength, comparing the experimental data (black circles), linked by a guideline, to the simulated results (gray squares). The blue triangle represents the simulated 3 PA case with an effective cross-section ~200 times smaller than the usual [79].

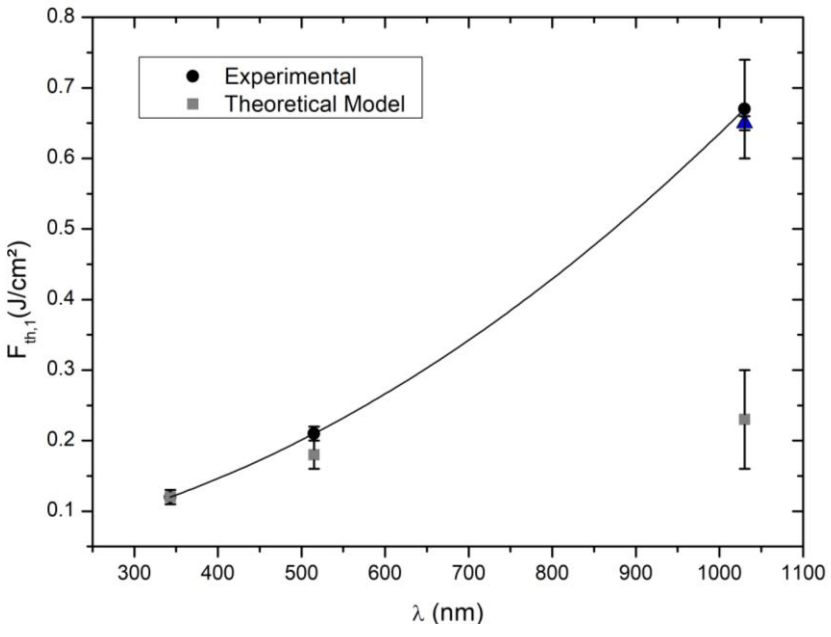

Source: by the author.

A first hypothesis for the effective cross-section was formed once the $F_{th,1}$ value experimentally determined at 1030 nm (0.67 J/cm^2), resulted in an intensity of I = 3.4 TW/cm^2. Therefore, micromachining in GaN is being performed in a regime of high-light intensity. Although excitation of an electron from the valence to the conduction band at 1030 nm is carried out by three-photons absorption (3 PA) in GaN, for the high-intensity regime (~1-10 TW/cm^2) the dynamics of the carrier excitation is such that recombination and, therefore, the near band edge (NBE) emission is favored due to the saturation of the defect levels, which results in a fourth-order dependence of the NBE emission on the excitation intensity, as shown by Martins, et al.[80], for excitation at 775 nm, where the population dynamics in GaN's valence and conduction band was modeled considering the addition of defect levels.

Yet according to Martins, et al.[80], the actual NBE emission observed in this high-intensity regime in Fig. 27 (red dashed line) is about 100-1000 times higher than what would be expected by simply extrapolating the low-intensity regime (~10-100 GW/cm^2) behavior, represented by the dashed blue line in Fig. 27, that follows a third-order dependence on the intensity, to the high-intensity one.

Figure 27 – NBE emission (red dashed line) and yellow emission (black dashed line) as function of the excitation intensity for GaN at a wavelength of 775 nm.

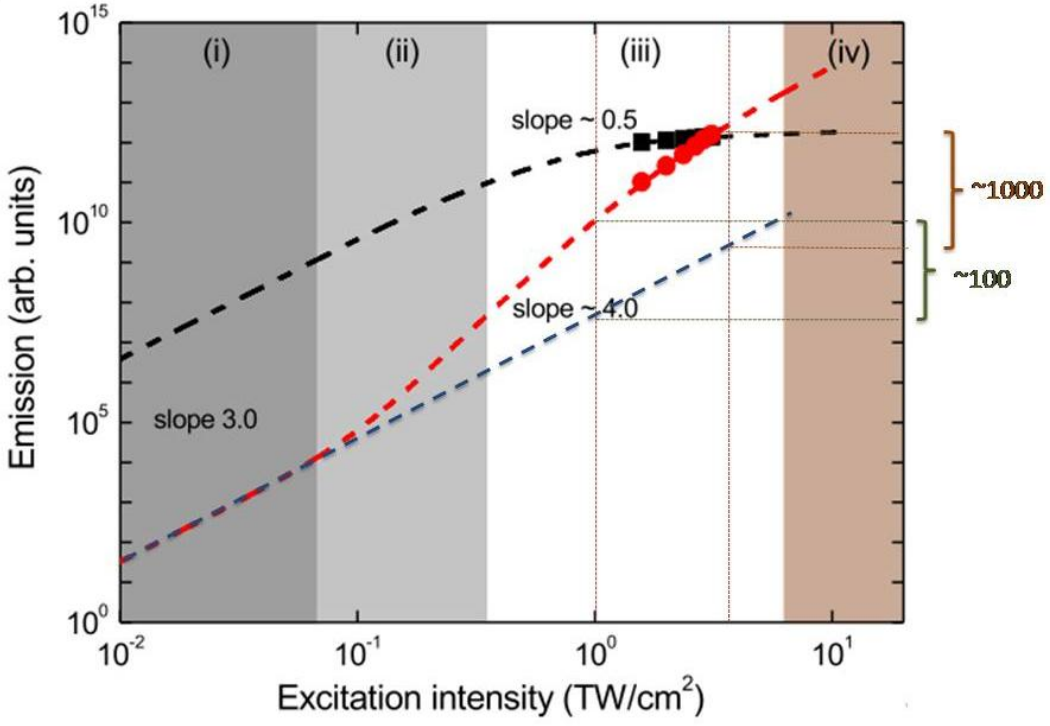

Source: adapted from Martins, et al.[80].

As a consequence, in such intensity regime the population of the conduction band is decreased by a factor of 100-1000, which can alternatively be described as a 3 PA process with an effective cross-section 100-1000 times smaller than the ones observed in the lower intensity regime (~10-100 GW/cm^2). Such interpretation could explain the effective 3 PA cross-section value used to describe the data in Fig. 26. However, this explanation is only true for a much longer period of time, requiring multiple fs-pulses instead of a single one, as proposed by the theoretical model.

A more suitable hypothesis for the discrepancy of the results at 1030 nm can be given trough the analysis of the Keldysh parameter from Eq. 2.17. As discussed previously in section 2.2, for γ_K significantly higher than one, multiphoton ionization prevails over the tunneling ionization. That is the case at 343 and 515 nm, where we determined γ_K of 27 and 12, respectively. In such situation, multiphoton ionization is the dominant mechanism and, therefore, it is in agreement with the model used to interpret the data. At 1030 nm, however, we obtained γ_K ~ 3, indicating an intermediate regime in which tunneling is also contributing, together with multiphoton absorption, to the nonlinear ionization of electrons, which is not taken into account in the model used interpret the data of Fig. 26. Hence, our results reveal that, at 1030 nm, micromachining of GaN presents contributions from both multiphoton and tunneling for the ionization.

4.2. CVD diamond

For the CVD diamond, we followed the same procedure from section 3.2 and 4.1: we determined the fluence threshold for all available wavelengths (343, 515 and 1030 nm) alongside the number of pulse superposition (from N = 1 to about 10^4) utilizing the zero damage method and Eqs. 4.1 and 4.2. Finally, we plotted the experimental data obtained of $F_{th,N}$ as function of N in order to evaluate the cumulative behavior of the incubation effect, seen in Figs. 29-31.

Figure 28 displays one example of the many graphs necessary for the study of the incubation effect. It reveals the relationship between the squared half-width of the micromachined lines as a function of the pulse energy, correctly predicted by Eq. 3.4, used as the fitting (dashed line) for about one hundred 1030 nm pulse superposition on the CVD diamond sample, from which we determined the

minimal laser fluence to produce damage to be (0.22 ± 0.05) J/cm^2 and the Gaussian beam waist at the focus w_0 = (1.5 ± 0.1) µm.

Figure 28 – Squared half-width of micromachined lines as function of the pulse energy of CVD diamond for about ten thousand 1030 nm pulses.

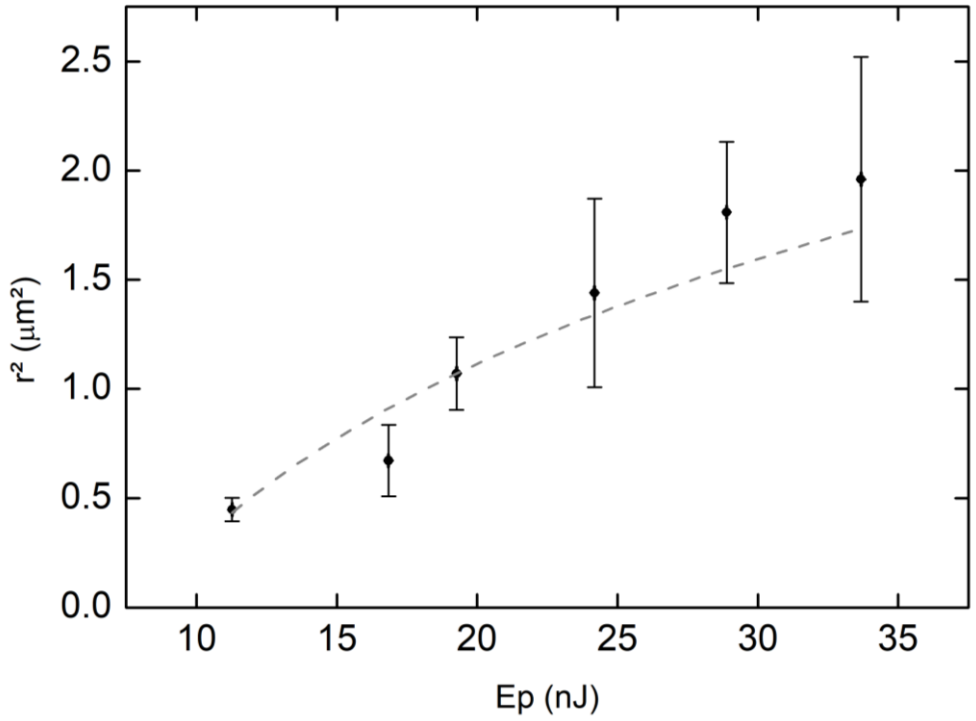

Source: by the author.

Figure 29 presents the incubation cumulative effect during the fs-micromachining of the CVD diamond sample at 1030 nm – a five-photon absorption process. As it can be noted from the threshold fluences as function of the pulse superposition number, much like GaN, the diamond sample presents the saturation of the defect generation at the high pulse superposition region, defined by the $F_{th,\infty}$. As such, Eq. 4.4 was used to fit the collected experimental data, represented by the dashed grey line. From the graph, a sizable decrease of $F_{th,N}$ is observed: from (2.3 ± 0.3) J/cm² to (0.20 ± 0.03) J/cm² in about 30 pulses per spot. This corroborates the incubation premise of a decrease in the damage threshold fluence with the defect generation before the ablation process takes place, which also increases due to the number of pulse superposition.

Figure 29 – Damage threshold fluence as function of pulse superposition of CVD diamond with 1030 nm laser pulses.

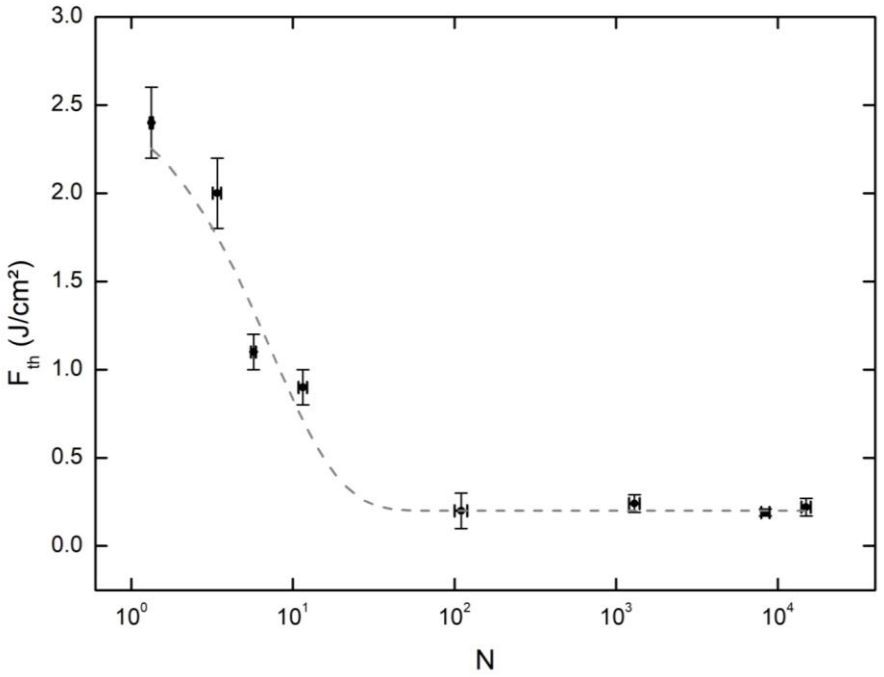

Source: by the author.

In Fig. 30, we display the damage threshold fluence of CVD diamond as a function of the applied number of pulses per spot at 515 nm, a three-photon absorption process, demonstrating the incubation effect.

Figure 30 – Damage threshold fluence as function of pulse superposition of CVD diamond with 515 nm laser pulses.

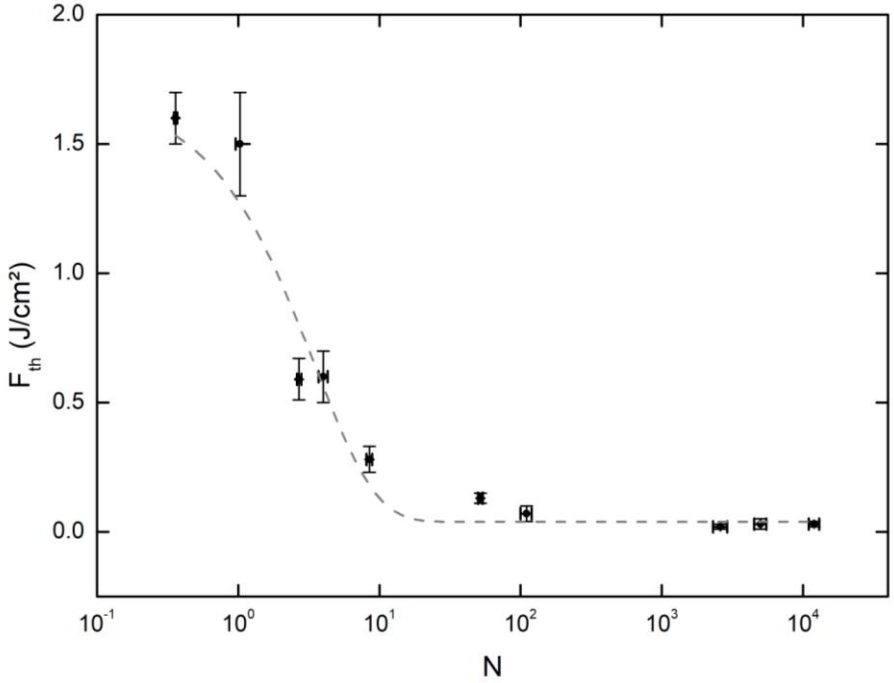

Source: by the author.

The $F_{th,N}$ values were determined through a graph of the squared half-width of the micromachined grooves in function of the pulse energy, and the number of pulses applied per spot was determined by Eqs. 4.1 and 4.2. Like in Fig. 29, there is a decrease in the $F_{th,N}$ from (1.3 ± 0.2) J/cm² to (0.03 ± 0.01) J/cm² in about 20 pulses, a behavior in agreement to the incubation proposition. When comparing the experimentally obtained fluence threshold data of the 1030 nm and 515 nm cases, it is clear that the values are overall greater in the IR excitation (1030 nm). This could be attributed to the difference in the number of photons present in the multiphoton absorption process involved in both cases: from 5 PA to a 3 PA process.

Finally, Fig. 31 presents the incubation cumulative process during the femtosecond micromachining of CVD diamond at 343 nm, for pulses of 216 fs of duration – a 2-photon absorption process.

Figure 31 – Damage threshold fluence as function of pulse superposition of CVD diamond with 343 nm laser pulses.

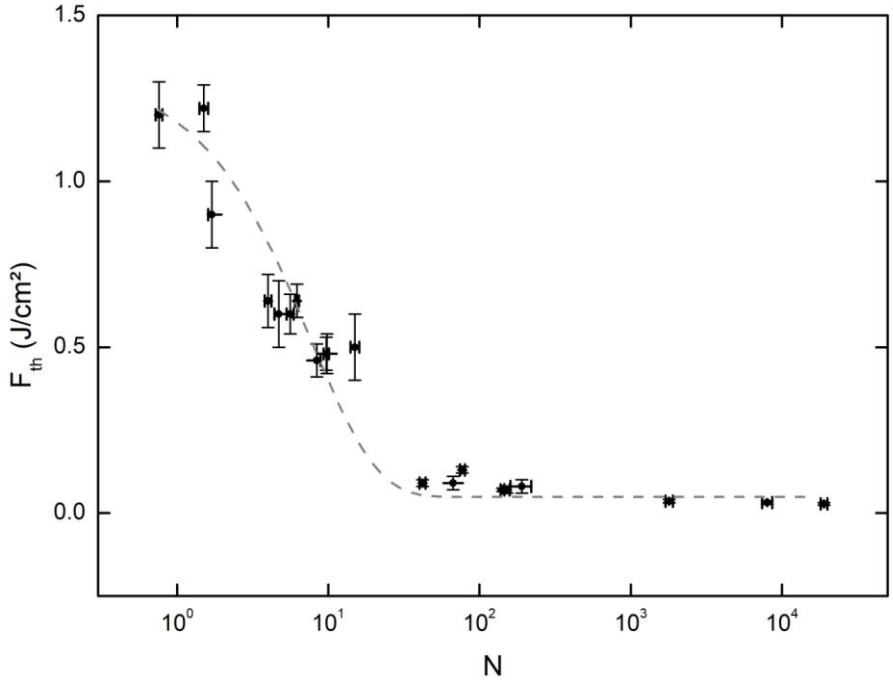

Source: by the author.

As the number of applied pulses per spot at 343 nm of the CVD diamond sample was increased, the threshold fluence decreased from (1.2 ± 0.2) J/cm² to (0.05 ± 0.01) J/cm², as the incubation effect dictates. Comparing the threshold fluence to the previous cases, the 5 PA process at 1030 nm is still the one with the highest overall values, followed by the 515 nm case (3 PA), which is slightly

bigger than the 343 nm case. Thus, as in GaN, this could be explained by the difference in the ionization processes present during the fs-micromachining: from a five-photon process at 1030 nm, to a three-photon at 515 nm and finally a two-photon nonlinear ionization process at 343 nm.

For the IR (1030 nm) case, about 30 pulses per spot were needed to drastically decrease the threshold fluence from (2.3 ± 0.3) J/cm² to (0.20 ± 0.03) J/cm², similarly to the UV wavelength (343 nm), decreasing from (1.2 ± 0.2) J/cm² to (0.05 ± 0.01) J/cm² in the same region. On the other hand, the green excitation wavelength (515 nm) required ~20 pulses to decrease from (1.3 ± 0.2) J/cm² to (0.03 ± 0.01) J/cm². This phenomenon can be explored in Fig. 32 through a graph of the incubation parameter (k) as function of the excitation wavelength.

Figure 32 – Incubation parameter *k* obtained from the incubation curves of CVD diamond as function of the applied wavelength linked by a guideline (black line).

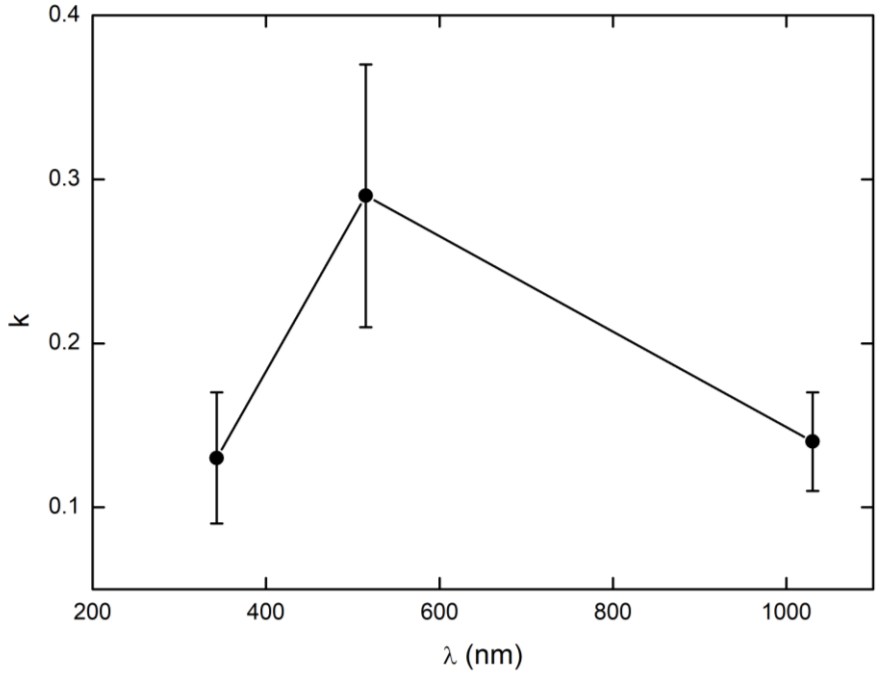

Source: by the author.

From the graph, we can see that k = (0.14 ± 0.03) at 1030 nm, k = (0.3 ± 0.1) at 515 nm, and finally k = (0.13 ± 0.04) at 343 nm. Thus, according to the definition of the incubation parameter, the excitation at 515 nm is more efficient than the 1030 nm and 343 nm cases to achieve the low-fluence plateau defined by the $F_{th,\infty}$ value. A possible explanation to this behavior may be due to the Nitrogen-Vacancy (NV) centers present in diamond, known to be excited at 532 nm[81]. Thus, it

might be possible that when excited at 515 nm, the NV centers would partially absorb the incident light (through linear absorption), facilitating the local ionization process. This alternative absorption would then lead to the micromachining process, which would be more efficient than a two, five or a regular three-photon absorption mechanism.

Utilizing the theoretical model discussed in the previous section, we made a numerical simulation of the electron number density as function of the laser peak intensity, given by Figs. 34-37. As in the GaN case, we also determined its Keldysh parameter, which resulted in values $\gg 1$ (γ_K = 23, 63 and 99 at 1030, 515 and 343 nm respectively), corroborating the fact that the multiphoton absorption process is present during the experiment.

Similarly to the GaN theoretical predictions, the number of photons involved in the absorption process (m) was determined by the diamond's energy gap (5.47 eV), resulting in m = 2, 3 and 5 photons for 343, 515 and 1030 nm respectively, according to Fig. 33. Given the fact that an electron can only be promoted to the conduction band (CB) from the valence band (VB), represented by the gray rectangles, if it is excited with energy greater than the energy gap, then when we apply photons (represented by straight arrows with sizes proportional to their energy) of 343 nm, it is clear that 2 photons are required to surpass the gap. In the 515 nm case, 3 photons are necessary (not taken into account a contribution from the NV defect centers as mentioned previously) and finally at 1030 nm, a five-photon absorption process takes place.

Figure 33 – Two-photon absorption for 343 nm (a), three-photon absorption for 515 nm (b) and five-photon absorption for 1030 nm (c), considering bandgap (energy gap between the valence band, VB, and conduction band, CB) of 5.47 eV for the diamond.

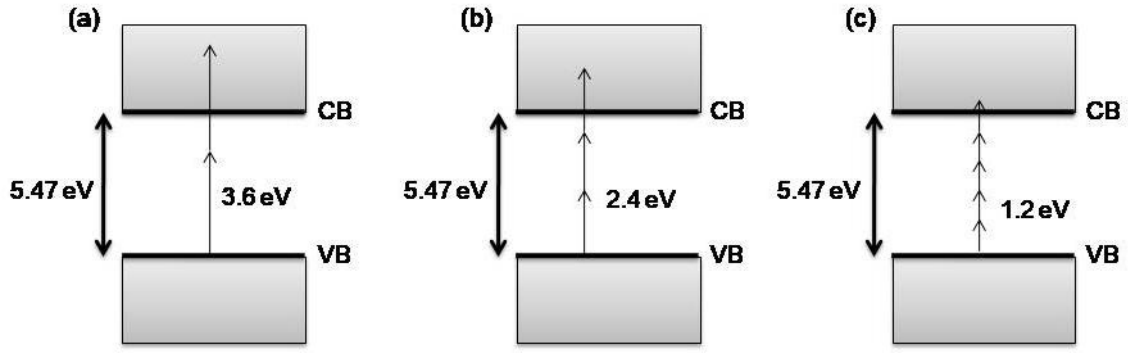

Source: by the author.

Figure 34 displays the graph of the simulated electron density (n) generated by fs-micromachining of the CVD diamond sample at 343 nm (2 PA process), with 216 fs pulses utilizing Eq. 4.6, as a function of the peak laser intensity I_0. As explained previously, for the UV case (343 nm), m = 2. Thus, a two-photon absorption cross-section was determined, trough Eq. 4.9, to be σ_2 = (7 ± 3) ×10^{-60} m^{4}s^{1}photon^{-1}, given the two-photon absorption coefficient found in the literature for CVD diamond[82]. As in the GaN case, Eq. 4.8 was used to calculate the solid atom density (Ns) of diamond. As its molecular mass is M = 12.01 g/mol and its density is d = 3.51 g/cm³ at 300 K[83], then Ns = 1.75×10^{29} m^{-3}. Finally, through this graph at 343 nm, we determined the optimal critical electron density which would lead to a value of I_0 responsible to recreate de experimental single-pulse threshold fluence obtained. Thus, the value n_{cr} = 6.4×10^{29} electrons/m^3 was determined, and utilized for the 515 nm and 1030 nm theoretical predictions for consistency. Thus, from the graph of Fig. 34, we computed $F_{th,1}$ = (1.20 ± 0.07) J/cm², equivalent to the experimental data $F_{th,1}$ = (1.2 ± 0.2) J/cm² (self-consistence).

Figure 34 – Electron density as function of the Gaussian peak intensity of diamond at λ = 343 nm, Ns = 1.75×10^{29} m^{-3} , σ_2 = (7 ± 3) ×10^{-60} m^{4}s^{1}photon^{-1} [82] and α = 10^{-3} m²/J [76]. The dashed red lines represent the curve associated error.

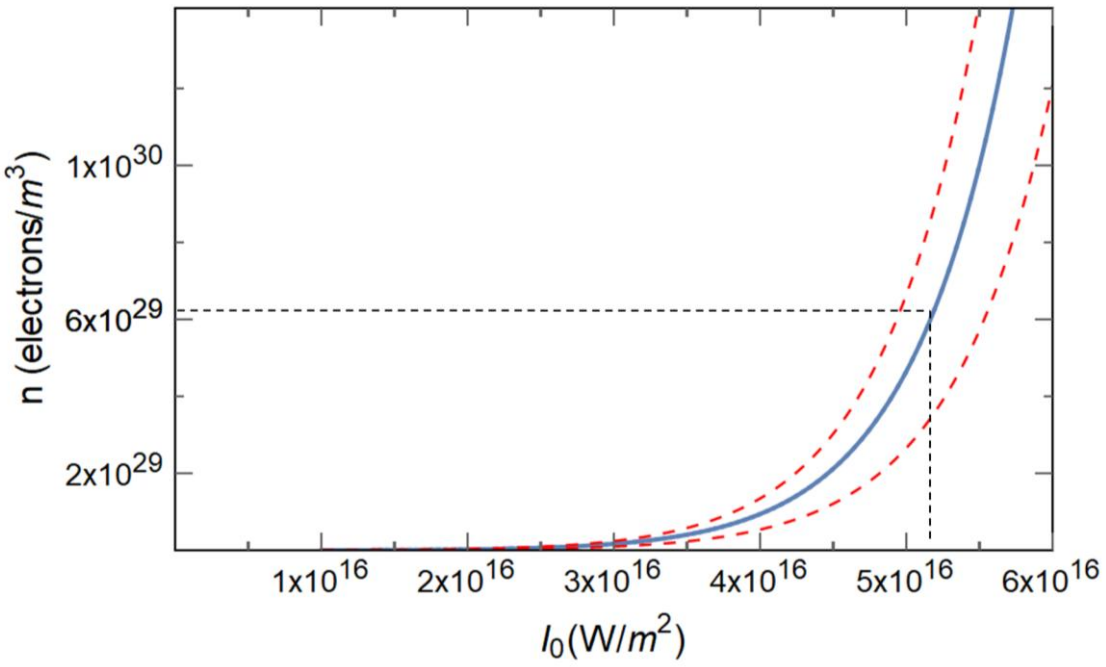

Source: by the author.

In Fig. 35, the electron density (n) was determined in the range of I_0 =

1×10^{16} W/m² up to I_0 = 4.5×10^{16} W/m² through Eq. 4.6 with 216 fs pulses at 515 nm – a three-photon absorption process. As such, the determination of a three-photon absorption cross-section is required. Thus, we utilized a three-photon absorption coefficient found for CVD diamond at 400 nm[70], given the lack of experimental data in the literature for 515 nm, resulting in $\sigma_3 = 3.2\times10^{-94}$ $m^6s^2photon^{-2}$. Finally, the parameter I_0 for which $n = n_{cr}$, illustrated by the crossing of the dashed black lines, was determined as I_0 = 3.9×10^{16} W/m². In contrast to the 343 nm case, the electron density at 515 nm does not present an associated error, due to the fact that the error (illustrated by the red dashed lines in Fig. 34) is originated from the uncertainty of the absorption coefficient, which was not reported for the 400 nm case[70].

Figure 35 – Electron density as function of the Gaussian peak intensity of diamond at λ = 515 nm, Ns = 1.75×10^{29} m^{-3} , $\sigma_3 = 3.2\times10^{-94}$ $m^6s^2photon^{-2}$ [70] and $\alpha = 10^{-3}$ m²/J [76].

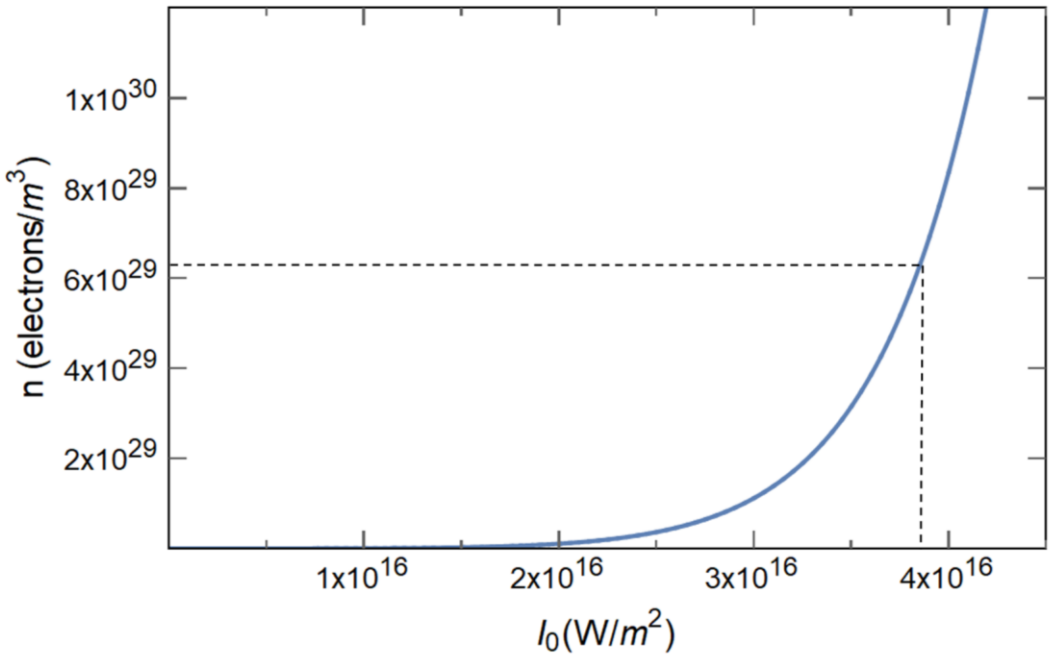

Source: by the author.

Even though the $F_{th,1}$ obtained for the 515 nm (3 PA), was determined through a value of cross-section for 400 nm, it can be considered a good fit ($F_{th,1}$ = 0.9 J/cm² is equivalent to the experimental value of $F_{th,1}$ = (1.3 ± 0.2) J/cm²), as shown in Table 1, where we compare the theoretical values of $F_{th,1}$ (obtained with the n_{cr} value optimized to the 343 nm case) to the experimental data.

Table 1 – Experimental and theoretical threshold fluence of a single pulse.

	Experimental $F_{th,1}$ (J/cm²)	Theoretical $F_{th,1}$ (J/cm²)
2 PA (343 nm)	1.2 ± 0.2	1.20 ± 0.07
3 PA (515 nm)	1.3 ± 0.2	0.9

Source: by the author.

Alternatively, we can compare the 515 nm results in a different approach: given the experimental damage threshold fluence of $F_{th,1}$ = (1.3 ± 0.2) J/cm², we determine the optimal I_0 necessary to result in an equivalent $F_{th,1}$ given by Eq. 4.5, assuming the same parameter of n_{cr} already defined. Thus, we can determine the three-photon absorption cross-section and compare it to σ_3 = 3.2×10^{-94} m^{6}s^{2}photon^{-2}, calculated via the 3 PA coefficient[70]. As such, we found a peak laser intensity of I_0 = 5.5×10^{16} W/m², which results in a threshold fluence of $F_{th,1}$ = 1.3 J/cm². Thus, through the graph of Fig. 36, we determined that an σ_3 = 0.18×10^{-94} m^{6}s^{2}photon^{-2} absorption cross-section was necessary to reach the I_0 and $n = n_{cr}$ pair given by Eq. 4.6 represented by the crossing of the black dashed lines.

Figure 36 – Electron density as function of the Gaussian peak intensity of diamond at λ = 515 nm, Ns = 1.75×10^{29} m^{-3} , σ_3 = 0.18×10^{-94} m^{6}s^{2}photon^{-2} and α = 10^{-3} m²/J [76].

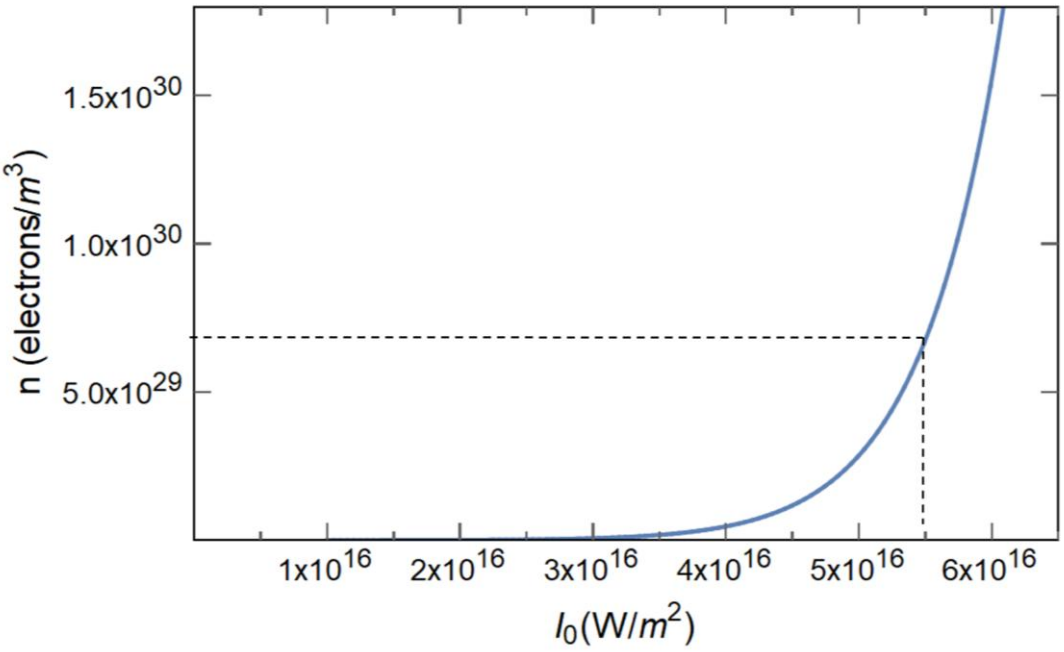

Source: by the author.

Therefore, given the fact that the three-photon absorption coefficient

obtained through the theoretical model was of the same order of the value determined through Eq. 4.9, we can affirm that the experimental data and the model are in good agreement. Even further, this theoretical model can be used as an alternative method to determine the m-photon absorption coefficient of a given material.

Lastly, in the infrared wavelength excitation case (1030 nm) there is an absence of data on the five-photon absorption cross-section for diamond in the literature. Thus, instead of determining the single pulse threshold fluence, we will calculate the five-photon absorption cross-section, by applying the same method described before: we will establish an optimal I_0 value to result in an equivalent single-pulse damage threshold fluence provided by Eq. 4.5, and then find what 5-photon cross-section (σ_5) can generate the pair n_{cr} and correspondent I_0. Thus, we determined I_0 = 9×10^{16} W/m², which results in $F_{th,1}$ = 2.1 J/cm², equivalent to the experimental $F_{th,1}$ = (2.3 ± 0.3) J/cm² and through the graph of Fig. 37 the optimal 5 PA cross-section (given our chosen parameters) is σ_5 = 5×10^{-170} m^{10}s^{4}photon^{-4}.

Figure 37 – Electron density as function of the Gaussian peak intensity of diamond at λ = 1030 nm, Ns = 1.75×10^{29} m^{-3} , σ_5 = 5×10^{-170} m^{10}s^{4}photon^{-4} and α = 10^{-3} m²/J [76].

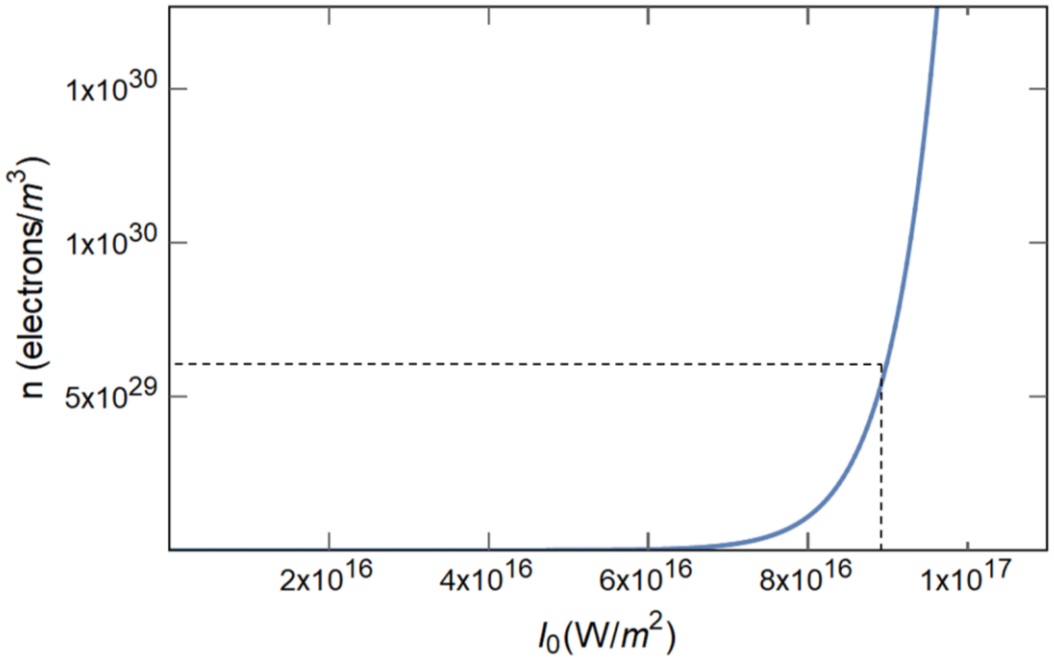

Source: by the author.

In order to have a better idea of the obtained value scale of the 5 PA cross-section of diamond, we can compare it to the value found for other materials,

seen in Table 2. On the second line of Table 2, we present the reported five-photon absorption cross-section of a TeO_2 based glass[84] at 1550 nm, a material known for its high nonlinear refractive index .

Table 2 – 5-PA cross-section overall comparison.

	λ (nm)	σ_5 ($cm^{10}s^4photon^{-4}$)
CVD diamond	1030	5×10^{-150}
TeO_2 based glass[84]	1550	2.6×10^{-144}
PDNB[85]	314	0.02×10^{-150}
IPPS[86]	2100	1.92×10^{-143}
Halide Perovskite Colloidal nanocrystals[87]	2050-2300	$\sim 10^{-136}$

Source: by the author.

Next on Table 2, the 5-PA cross-section is present at 314 nm[85] for p-dinitrobenzene (PDNB), a centrosymmetric organic molecule whose molecular structure can be seen in Fig. 38.

Figure 38 – Molecular structure of p-dinitrobenzene (PDNB).

Source: adapted from Friese, et al.[85].

In the fourth line of Table 2, (E)-3-(4-(2-(1-hexyl-4-methyl-1H-imidazol5-yl)vinyl)pyridinium-1-yl)propyl sulphate (IPPS), seen in Fig. 39, has its 5 PA cross-section reported at 2100 nm[86]. Lastly, the large five-photon absorption cross-section of Halide Perovskite Colloidal nanocrystals[87], a semiconductor material, can be seen in the 5th line at 2050-2300 nm.

Figure 39 – Molecular structure of (E)-3-(4-(2-(1-hexyl-4-methyl-1H-imidazol5-yl)vinyl)pyridinium-1-yl)propyl sulphate (IPPS).

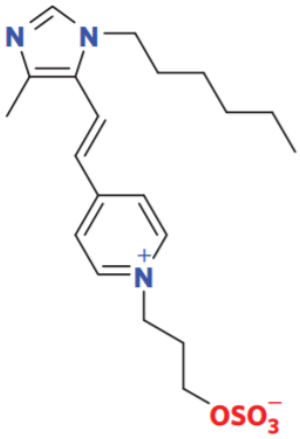

Source: adapted from Zheng, et al.[86].

Even though the comparison of the five-photon absorption cross-section determined for diamond at 1030 nm to other types of materials at different wavelengths is not straightforward, it is clear that the result we determined is consistent to the other 5 PA reported. The difference in the order of magnitude can be attributed to the considerably bigger molecular sizes of the organic materials or to atypical behavior, as in the Halide Perovskite Colloidal nanocrystals case[87]. At the same time, our 5 PA cross-section value is on the same order of PDNB[85], indicating that the determined value could be, in fact, a good prediction.

5. CONCLUSIONS AND PERSPECTIVES

In this dissertation, we have studied the fundamentals involved in the femtosecond laser micromachining at different wavelengths (343, 515 and 1030 nm), more specifically the incubation effect, as well as the nonlinear processes involved in both GaN and CVD diamond. To achieve that, we employed the zero damage technique to obtain the damage threshold fluences. With the experimental data collected, we were able to study the cumulative behavior of the incubation effect of GaN and CVD diamond from graphs of the $F_{th,N}$ in function of the pulse superposition number. From that, we were able to perceive that with the increase of the pulse superposition, the damage fluence decreases until it reaches a plateau of the minimal fluence value. The efficiency by which the fluences arrive at that plateau differs for every excitation wavelength. This is measured by the incubation parameter (k): the higher its value, fewer pulses are required to reach the bottom saturation of the graph. In GaN, for instance, the parameter k has a decreasing behavior to the applied wavelength: k = (0.4 ± 0.2) for 343 nm, k = (0.07 ± 0.01) for the green and k = (0.02 ± 0.01) for the IR case. CVD diamond, on the other hand, does not present a similar nature: k = (0.13 ± 0.04) for the UV, k = (0.3 ± 0.1) for 515 nm and k = (0.14 ± 0.03) for the 1030 nm excitation wavelength. Thus, the incubation effect is more pronounced when applying 343 nm femtosecond pulses in GaN while for the CVD diamond, 515 nm is a better suit. Therefore, knowledge of the incubation effect and how it behaves under different wavelengths is essential for the processing of materials by femtosecond laser pulses, as not only does it reveal which wavelength could be more effective for an specific material, but also depending on the fs-laser system available for a given experiment, one could consult the incubation graph to determine the damage threshold fluence at a certain number of pulses, thus increasing the experiment resolution, as the fs-micromachined groove width is smaller when operating near this value.

In addition, a theoretical model was used to compare results of the single pulse damage threshold fluence to our experimental data. The model assumes that only multiphoton and avalanche absorption processes are in place during the fs-micromachining of the material. Then, through the simulation of the density number of electrons in function of the laser peak intensity, we were able to determine the

single pulse damage threshold values of GaN for 343, 515 and 1030 nm. The model matches with the 1 and 2 photon absorption case (343 and 515 nm), but does not agree with the result of 1030 nm. This was explained once we determined the Keldysh parameter for all experimental data, which resulted in values ≫ 1 in the 343 and 515 nm cases, while at 1030 nm, γ_K ~ 3, indicating that both tunneling and multiphoton ionization were responsible for the electron plasma generation – a phenomenon that was not considered by the theoretical model.

Finally, we performed the same method in the CVD diamond sample: by finding the optimal n_{cr} at the 343 nm case, we determined the threshold fluence for the two and three-photon absorption process (343 nm and 515 nm respectively). As the found values were in good agreement to the experimental results, we compared the model to the experimental data with a different approach. Instead of determining the peak intensity for which $n = n_{cr}$ and then calculating the single-pulse threshold fluence, we established a I_0 necessary to reproduce the experimental $F_{th,1}$ data. Thus, we determined what value of m-photon absorption cross-section was necessary for the pair n_{cr} and I_0 to occur. With this alternative method, we determined a 3 PA cross-section of the CVD diamond at 515 nm to be $\sigma_3 = 0.18\times10^{-94}$ $m^6s^2photon^{-2}$**,** which is of the same order of magnitude of the amount found in the literature. This alternative method came in use when in the 1030 nm case (5 PA process), the 5 PA cross-section was not found in the literature. Thus, by applying the procedure described beforehand, we determined the five-photon absorption cross-section of $\sigma_5 = 5\times10^{-170}$ $m^{10}s^4photon^{-4}$, which is consistent to values reported for other materials.

Hence, this study could improve the femtosecond micromachining processing of both GaN and diamond, with a better understanding of its fundamental processes, in both a practical and theoretical approach. Besides what was accomplished in this dissertation, we look forward to analyze the incubation cumulative effect in other materials of technological interest, as the behavior can change depending on the material, and its knowledge is of great importance from the fs-micromachining point of view. In addition, as the theoretical model proved to be an alternative method of determining the m-photon absorption cross-section, further tests should be employed to prove its efficacy. A more direct approach would be the direct measurements of the 3 and 5 PA cross-section of diamond, which could be

made by the Z-Scan method, which consists of analyzing the normalized transmittance of the sample while it is translated along the laser propagation direction[88].

REFERENCES

1 SAMAD,R. E. et al. Ultrashort laser pulses machining.*In*: PESHKO, I. (Ed.). **Laserpulses** - theory, technology, and applications. 2012. Cap. 5, p. 143-174. DOI: http://dx.doi.org/10.5772/46235.

2 KRÜGER, J.; KAUTEK, W. Ultrashort pulse laser interaction with dielectrics and polymers. **Advances in Polymer Science**, v. 168, p. 247–289, 2004.

3 KAMINSKI, P. C.; CAPUANO, M. N. Micro hole machining by conventional penetration electrical discharge machine. **International Journal of Machine Tools and Manufacture**, v. 43, n. 11, p. 1143–1149, 2003.

4 PRADHAN, B. B. et al. Investigation of electro-discharge micro-machining of titanium super alloy. **International Journal of Advanced Manufacturing Technology**, v. 41, n. 11–12, p. 1094–1106, 2009.

5 LANGFORD, R. M. et al. Focused ion beam micromachining of three-dimensional structures and three-dimensional reconstruction to assess their shape. **Journal of Micromechanics and Microengineering**, v. 12, n. 2, p. 111–114, 2002.

6 LAPOINTE, J. et al. Making smart phones smarter with photonics. **Optics Express**, v. 22, n. 13, p. 15473, 2014.

7 MAIMAN, T. H. Stimulated optical emission in ruby. **Journal of the Optical Society of America**, v. 50, n. 11, p. 1134, 1960.

8 CERAMI, L. et al. Femtosecond laser micromachining. **Ultrafast Nonlinear Optics**, p. 287–321, 2013.

9 YODER, M. N. Wide bandgap semiconductor materials and devices. **IEEE Transactions on Electron Devices**, v. 43, n. 10, p. 1633–1636, 1996.

10 HUDGINS, J. L. et al. An Assessment of wide bandgap semiconductors for power devices. **IEEE Transactions on Power Electronics**, v. 18, n. 3, p. 907–914, 2003.

11 KIM, T. et al. Femtosecond laser machining of gallium nitride. *In*: ANNUAL MEETING CONFERENCE PROCEEDINGS - LASERS AND ELECTRO-OPTICS SOCIETY, 13., 2000, Rio Grande. **Proceedings [...]**. Picastaway: IEEE, 2000. v. 2, p. 565–566. DOI: 10.1109/LEOS.2000.893967.

12 GUOSHENG, Z.; FAUCHET, P. M.; SIEGMAN, A. E. Growth of spontaneous periodic surface structures on solids during laser illumination. **Physical Review B**, v. 26, n. 10, p. 5366–5381, 1982.

13 VAN DRIEL, H. M.; SIPE, J. E.; YOUNG, J. F. Laser-induced periodic surface structure on solids: A universal phenomenon. **Physical Review Letters**, v. 49,

n. 26, p. 1955–1958, 1982.

14 HUANG, M. et al. Origin of laser-induced near-subwavelength ripples: Interference between surface plasmons and incident laser. **ACS Nano**, v. 3, n. 12, p. 4062–4070, 2009.

15 ECHLIN, M. P. et al. Materials response to glancing incidence femtosecond laser ablation. **Acta Materialia**, v. 124, p. 37–46, 2017.

16 STOLZ, A. et al. Prospective for gallium nitride-based opticalwaveguide modulators. **IEICE Transactions on Electronics**, v. E95-C, n. 8, p. 1363–1368, 2012.

17 ZHANG, Y. et al. GaN directional couplers for integrated quantum photonics. **Applied Physics Letters**, v. 99, n. 16, p. 161119, 2011.

18 HUI, R. et al. Gan-based waveguide devices for long-wavelength optical communications. **Applied Physics Letters**, v. 82, n. 9, p. 1326–1328, 2003.

19 WESTREICH, O. et al. Low propagation loss in GaN/AlGaN-based ridge waveguides. **Physica Status Solidi (A) Applications and Materials Science**, v. 212, n. 5, p. 1043–1048, 2015.

20 HALSTUCH, A. et al. Femtosecond laser inscription of Bragg gratings on a thin GaN film grown on a sapphire substrate. **Optics and Lasers in Engineering**, v. 109, p. 68–72, 2018.

21 ALMEIDA, G. F. B. et al. Incubation effect during laser micromachining of GaN films with femtosecond pulses. **Journal of Materials Science: Materials in Electronics**, v. 30, n. 18, p. 16821–16826, 2019.

22 SHIRK, M. D. et al. Ultrashort-pulsed laser microstructuring of diamond. *In*: INTERNATIONAL SYMPOSIUM ON LASER PRECISION MICROFABRICATION, 2000, Omiya. **Proceedins [...]**. v. 4088, p. 98–101. DOI: https://doi.org/10.1117/12.405693.

23 DOU, J. et al. Process research on micro-machining diamond microgroove by femtosecond laser. **Integrated Ferroelectrics**, v. 198, n. 1, p. 9–19, 2019.

24 KONONENKO, T. V. et al. Microstructuring of diamond bulk by IR femtosecond laser pulses. **Applied Physics A**: materials science and processing, v. 90, n. 4, p. 645–651, 2008.

25 SUN, Y. et al. Research on the mechanism of micromachining of CVD diamond by femtosecond laser. **Ferroelectrics**, v. 549, n. 1, p. 266–275, 2019.

26 SHIVAKUMAR, V. B. et al. Femtosecond laser written diamond waveguides: a step towards integrated photonics in the far infrared. **Optical Materials**, v. 85, p.183-185, 2018. DOI: 10.1016/j.optmat.2018.08.062.

27 TERASAWA, E. et al. Pulse duration dependence of ablation threshold for fused silica in the visible femtosecond regime. **Applied Physics A**: materials science and processing, v. 126, n. 6, 2020. DOI: https://doi.org/10.1007/s.0039-020-03640-0.

28 IPPEN, E. P. Principles of passive mode locking. **Applied Physics B**: laser and optics, v. 58, n. 3, p. 159–170, 1994.

29 DUCASSE, A.; RULLIÈRE, C.; COUILLAUD, B. Methods for the generation of ultrashort laser pulses: mode-locking. *In*: RULLIÈRE, C. (Ed.). **Femtosecond laser pulses**. New York: Springer-Verlag, 1998. p. 53–82.

30 MOUROU, G.; STRICKLAND, D. Compression of amplified chirped optical pulses. **Optics Communications**, v. 56, n. 3, p. 219–221, 1985.

31 ASPLUND,M.C. et al. The 2018 Nobel Prize in Physics: optical tweezers and chirped pulse amplification. **Analytical and Bioanalytical Chemistry.** v.411, p.5001–5005, 2019.

32 BOYD, R.W. The Nonlinear optical susceptibility. *In*: BOYD, R. W. **Nonlinear optics**. 3rded. New York: Academic Press, 2008.p. 1–12.

33 AMS, M. et al. Investigation of ultrafast laser-photonic material interactions: Challenges for directly written glass photonics. **IEEE Journal on Selected Topics in Quantum Electronics**, v. 14, n. 5, p. 1370–1388, 2008.

34 BOYD, R. W. Quantum-mechanical theory of the nonlinear optical susceptibility.*In*: BOYD, R. W. **Nonlinear optics**. 3rded. New York: Academic Press, 2008.p. 135–204.

35 KELDYSH, L. V. Ionization in the field of a strong electromagnetic wave. **Soviet Physics JETP**, v. 20, n. 5, p. 1945–1957, 1965.

36 MARY, R.; CHOUDHURY, D.; KAR, A. K. Applications of fiber lasers for the development of compact photonic devices. **IEEE Journal on Selected Topics in Quantum Electronics**, v. 20, n. 5, p.1-3, 2014. DOI: 10.1109/JSTO.2014.2301136.

37 QUINTO-SU, P. A.; VENUGOPALAN, V. Mechanisms of laser cellular microsurgery. *In*: BERNS, M.. W.; GREULICH, K. O. **Laser manipulation of cells and tissues**. New York: Elsevier, 2007.p. 113-151. (Methods in Cell Biology, 82).

38 HERCHER, M. Laser-induced damage in transparent media. **Journal of the Optical Society of America**, v. 54, p. 563, 1964.

39 PRONKO, P. P. et al. Machining of sub-micron holes using a femtosecond laser at 800 nm. **Optics Communications**, v. 114, n. 1–2, p. 106–110, 1995.

40 KANAVIN, A. et al. Heat transport in metals irradiated by ultrashort laser

pulses. **Physical Review B** - condensed matter and materials physics, v. 57, n. 23, p. 14698–14703, 1998.

41 ANISIMOV, S. I.; KAPELIOV.BL; PERELMAN, T. L. Electron-emission from surface of metals induced by ultrashort laser pulses. **Zhurnal Eksperimentalnoi I Teoreticheskoi Fiziki**, v. 66, n. 2, p. 776–781, 1974.

42 LORAZO, P.; LEWIS, L. J.; MEUNIER, M. Short-pulse laser ablation of solids: from phase explosion to fragmentation. **Physical Review Letters**, v. 91, n. 22,p. 225502, 2003.

43 PEREZ, D.; LEWIS, L. J. Molecular-dynamics study of ablation of solids under femtosecond laser pulses. **Physical Review B** - condensed matter and materials physics, v. 67, n. 18, p. 184102, 2003.

44 ZHIGILEI, L. V. Dynamics of the plume formation and parameters of the ejected clusters in short-pulse laser ablation. **Applied Physics A**: materials science and processing, v. 76, n. 3, p. 339–350, 2003.

45 REIF, J.; COSTACHE, F. Femtosecond laser interaction with solid surfaces: explosive ablation and self-assembly of ordered nanostructures. *In*: REMPE, G.; SCULLY, M. (Ed.). **Advances in atomic, molecular and optical physics**. New York: Elsevier, 2006.v. 53, p. 227–251.

46 STOIAN, R. et al. Surface charging and impulsive ion ejection during ultrashort pulsed laser ablation. **Physical Review Letters**, v. 88, n. 9, p. 976031–976034, 2002.

47 BULGAKOVA, N. M. et al. A general continuum approach to describe fast electronic transport in pulsed laser irradiated materials: The problem of Coulomb explosion. **Applied Physics A**: materials science and processing, v. 81, n. 2, p. 345–356, 2005.

48 MERO, M. On the Damage behavior of dielectric films when illuminated with multiple femtosecond laser pulses. **Optical Engineering**, v. 44, n. 5, p. 051107, 2005.

49 COSTACHE, F.; ECKERT, S.; REIF, J. Near-damage threshold femtosecond laser irradiation of dielectric surfaces: desorbed ion kinetics and defect dynamics. **Applied Physics A**: materials science and processing, v. 92, n. 4, p. 897–902, 2008.

50 JEE, Y.; BECKER, M. F.; WALSER, R. M. Laser-induced damage on single-crystal metal surfaces. **Journal of the Optical Society of America B**, v. 5, n. 3, p. 648, 1988.

51 ASHKENASI, D. et al. Surface damage threshold and structuring of dielectrics using femtosecond laser pulses: the role of incubation. **Applied Surface Science**, v. 150, n. 1, p. 101–106, 1999.

52 MARTIN, S. et al. Spot-size dependence of the ablation threshold in dielectrics for femtosecond laser pulses. **Applied Physics A**: materials science and processing, v. 77, n. 7, p. 883–884, 2003.

53 LIU, J. M. Simple technique for measurements of pulsed gaussian-beam spot sizes. **Optics Letters**, v. 7, n. 5, p. 196, 1982.

54 HUA, Q.; MA, B.; HU, W. Aluminum, gallium, and indium nitrides. **Reference Module in Materials Science and Materials Engineering**, p. 1–10, Mar. 2020.

55 PONCE, F. A.; BOUR, D. P. Nitride-based semiconductors for blue and green light-emitting devices. **Nature**, v. 386, n. 6623, p. 351–359, 1997.

56 PEARTON, S. J.; REN, F. GaN electronics. **Advanced Materials**, v. 12, n. 21, p. 1571–1580, 2000.

57 MORKOÇ, H.; CARLO, A. DI; CINGOLANI, R. GaN-based modulation doped FETs and UV detectors. **Solid-State Electronics**, v. 46, n. 2, p. 157–202, 2002.

58 HUANG, Y. et al. Gallium nitride nanowire nanodevices. **Nano Letters**, v. 2, n. 2, p. 101–104, 2002.

59 MIRAGLIOTTA, J.; WICKENDEN, D. K. Electroreflectance from gallium nitride using second-harmonic generation. **Materials Research Society Symposium** - Proceedings, v. 395, p. 541–546, 1996.

60 HUANG, Y. L. et al. Femtosecond Z-scan measurement of GaN. **Applied Physics Letters**, v. 75, n. 22, p. 3524–3526, 1999.

61 MATTOX, D. M. Thermal evaporation and deposition in vacuum. *In*: MATTOX, D. M. **The Foundations of vacuum coating technology**. New York: Elsevier, 2003.p. 151–184.

62 HILL, A. Growth, Characterization, and Thermodynamics of III-Nitride Semiconductors. Arizona State University, 2011.

63 WORT, C. J. H.; BALMER, R. S. Diamond as an electronic material. **Materials Today**, v. 11, n. 1–2, p. 22–28, 2008.

64 AHARONOVICH, I.; GREENTREE, A. D.; PRAWER, S. Diamond photonics. **Nature Photonics**, v. 5, n. 7, p. 397–405, 2011.

65 HAUSMANN, B. J. M. et al. Diamond nonlinear photonics. **Nature Photonics**, v. 8, n. 5, p. 369–374, 2014.

66 TILLEY, R. J. D. Color centers. **Encyclopedia of Color Science and Technology**, 2013. p. 1–9.

67 KIANINIA, M.; AHARONOVICH, I. Diamond photonics is scaling up. **Nature Photonics**, v. 14, n. 10, p. 599–600, 2020.

68 CALLISTER, W. D. J. Strucures and properties of ceramics. *In*: CALLISTER JR., W. D.; RELHWISCH, O. G. **Materials science and engineering an introduction**. 7th ed. New Yotk: John Wiley, 2007. p. 430-431.

69 KAMINSKII, A. A.; RALCHENKO, V. G.; KONOV, V. I. CVD-diamond - a novel χ(3)-nonlinear active crystalline material for SRS generation in very wide spectral range.**Laser Physics Letters**, v. 3, n. 4, p. 171–177, 2006.

70 KOZÁK, M. et al. Two- and three-photon absorption in chemical vapor deposition diamond. **Journal of the Optical Society of America B**, v. 29, n. 5, p. 1141, 2012.

71 Element Six. Diamond Handbook, 2020.

72 SCHWANDER, M.; PARTES, K. A Review of diamond synthesis by CVD processes. **Diamond and Related Materials**, v. 20, n. 9, p. 1287–1301, 2011.

73 MACHADO, L. M. et al. D-Scan measurement of ablation threshold incubation effects for ultrashort laser pulses. **Optics Express**, v. 20, n. 4, p. 4114, 2012.

74 OWEN, D. B.; ABRAMOWITZ, M.; STEGUN, I. A. Handbook of mathematical functions with formulas, graphs, and mathematical tables. **Technometrics**, v. 7, n. 1, p. 78, 1965.

75 SUN, Z.; LENZNER, M.; RUDOLPH, W. Generic incubation law for laser damage and ablation thresholds. **Journal of Applied Physics**, v. 117, n. 7, p. 073102, 2015.

76 STUART, B. et al. Nanosecond-to-femtosecond laser-induced breakdown in dielectrics. **Physical Review B** - condensed matter and materials physics, v. 53, n. 4, p. 1749–1761, 1996.

77 LEVINSHTEIN, M. E.; RUMYANTSEV, S. L.; SHUR, M. S. **Properties of Advanced semiconductor materials GaN,AlN,InN,BN,SiC,SiGe**. New York: John Wiley, 2001.

78 ALMEIDA, G. F. B. et al. Third-order nonlinear spectrum of GaN under femtosecond-pulse excitation from the visible to the near infrared. **Photonics**, v. 6, n. 2, p. 69, 2019.

79 VIVAS, M. G. et al. Nonlinear spectra of ZnO: reverse saturable, two- and three-photon absorption. **Optics Express**, v. 18, n. 9, p. 9628, 2010.

80 MARTINS, R. J. et al. Carrier dynamics and optical nonlinearities in a GaN epitaxial thin film under three-photon absorption. **Journal of Applied Physics**, v. 123, n. 24, p. 243101, 2018.

81 SUBEDI, S. et al. Laser spectroscopy of highly doped NV- centers in diamond. 2018. DOI: 10.1117/12.2290705.

82 ALMEIDA, J. M. P. et al. Nonlinear optical spectrum of diamond at femtosecond regime. **Scientific Reports**, v. 7, n. 1, p. 14320, 2017.

83 **NSM Archive - Diamond (C) - Basic Parameters**. Available at: <http://www.matprop.ru/Diamond_basic>. Acessed at : Sept. 10th 2020.

84 BINDRA, K. S. et al. Nonlinear optical properties of chalcogenide glasses: Observation of multiphoton absorption. **Applied Physics Letters**, v. 79, n. 13, p. 1939–1941, 2001.

85 FRIESE, D. H.; BAST, R.; RUUD, K. Five-photon absorption and selective enhancement of multiphoton absorption processes. **ACS Photonics**, v. 2, n. 5, p. 572–577, 2015.

86 ZHENG, Q. et al. Frequency-upconverted stimulated emission by simultaneous five-photon absorption. **Nature Photonics**, v. 7, n. 3, p. 234–239, 2013.

87 CHEN, W. et al. Giant five-photon absorption from multidimensional core-shell halide perovskite colloidal nanocrystals. **Nature Communications**, v. 8, p. 15198, 2017.

88 CHAPPLE, P. B. et al. Single-beam Z-scan: measurement techniques and analysis. **Journal of Nonlinear Optical Physics and Materials**, v. 6, n. 3, p. 251–293, 1997.